

# Mapping electrostatic potential in electrolyte solution

Bo Huang<sup>1†</sup>, Yining Yang<sup>2,3†</sup>, Ruinong Han<sup>4†</sup>, Keke Chen<sup>1†</sup>, Zhiyuan Wang<sup>2,3</sup>,  
Longteng Yun<sup>1</sup>, Yian Wang<sup>2,3</sup>, Haowei Chen<sup>1</sup>, Yingchao Du<sup>2,3</sup>, Yuxia Hao<sup>4</sup>, Peng Lv<sup>2,3</sup>,  
Haoran Ma<sup>1</sup>, Pengju Ji<sup>1</sup>, Yuemei Tan<sup>2,3</sup>, Lianmin Zheng<sup>2,3</sup>, Lihong Liu<sup>4\*</sup>, Renkai Li<sup>2,3\*</sup>,  
and Jie Yang<sup>1\*</sup>

## Affiliations:

<sup>1</sup> Center of Basic Molecular Science, Department of Chemistry, Tsinghua University; Beijing, China.

<sup>2</sup> Department of Engineering Physics, Tsinghua University; Beijing, China.

<sup>3</sup> Key Laboratory of Particle and Radiation Imaging, Tsinghua University, Ministry of Education, Beijing, China

<sup>4</sup> College of Chemistry, Beijing Normal University; Beijing, China.

\*Corresponding authors. Email: lihong.liu@bnu.edu.cn, lirk@tsinghua.edu.cn, jieyang1@tsinghua.edu.cn

†These authors contributed equally to this work.

## Abstract:

Mapping the electrostatic potential (ESP) distribution around ions in electrolyte solution is crucial for the establishment of a microscopic understanding of electrolyte solution properties. For solutions in the bulk phase, it has not been possible to measure the ESP distribution on Ångstrom scale. Here we show that liquid electron scattering experiment using state-of-the-art relativistic electron beam can be used to measure the Debye screening length of aqueous LiCl, KCl, and KI solutions across a wide range of concentrations. We observe that the Debye screening length is long-ranged at low concentration and short-ranged at high concentration, providing key insight into the decades-long debate over whether the impact of ions in water is long-ranged or short-ranged. In addition, we show that the measured ESP can be used to retrieve the non-local dielectric function of electrolyte solution, which can serve as a promising route to investigate the electrostatic origin of special ion effects. Our observations show that, interaction, as one of the two fundamental perspectives for understanding electrolyte solution, can provide much richer information than structure.

The macroscopic properties of electrolyte solutions are governed by the microscopic structure (i.e. how atoms and ions arrange themselves) and interaction (i.e. what forces do they feel). On the structure side, many well-established experimental techniques have successfully revealed the atomic arrangement in the electrolyte solution, often with sub-angstrom resolution, including but not limited to X-ray/neutron scattering, infrared spectroscopy, NMR spectroscopy, and EXAFS spectroscopy (1-8). Benefiting from these experimental techniques, key structural parameters, such as solvation shell radii and solvation numbers, have been determined with atomic-level precision. On the interaction side, while it is generally assumed that the interaction between ions and its solvation environment is primarily electrostatic in nature, it is very difficult to study experimentally. The famous Debye-Hückel (DH) model, proposed exactly a century ago in 1923, provides a classical description of electrostatic potential (ESP) distribution around ions in electrolyte solution (9). In the past century, it has only been possible to verify DH model experimentally on interface condition with few-nanometer length scale (10). To the best of our knowledge, there is no experimental method available for a direct measurement of ESP distribution at angstrom length scale in bulk solution.

Since the discovery of Hofmeister effect 150 years ago (11), the impact of ions in aqueous solution has generated strong interests. A particularly important question is whether this impact is long-ranged (i.e. beyond the first solvation shell), or short-ranged (i.e. within the first solvation shell). Because of that ions can influence bulk properties of water, such as viscosity, historically it is widely accepted that the impact of ions is long-ranged. This was later confirmed by Neutron and X-ray diffraction (6, 7, 12, 13) and dielectric relaxation spectroscopy (14, 15) experiments. Since early 2000, ultrafast vibrational spectroscopy experiments (16-18) have supported the opposite conclusion that the impact of ions in aqueous solution is mostly short-ranged, in sharp conflict with the long-standing view. These results have generated heated debate, and follow-up studies have shown a mixture of results, with some supporting short-ranged impact (19-21) and others supporting long-ranged impact (22-24). These studies, however, mostly rely on indirect spectroscopy probes and theoretical models. Given that ion interacts with surrounding environment primarily electrostatically, the experimental measurement of Debye screening length  $\lambda_D$ —a parameter that characterizes how far the ESP of an ion can propagate into the solvation environment—could serve as a direct answer to this question.

Scattering has been serving as a primary tool for determining the atomic structure of matter for over 100 years. Liquid electron scattering (LES) is recently enabled thanks to the latest advancements in relativistic electron sources and in-vacuum liquid sheet technologies (25, 26). So far, LES has been used for determining the static (27) and time-resolved liquid structure (28), in a similar fashion with X-ray and neutron scattering. In this study, we show that LES is capable of mapping the ESP distribution around ions in electrolyte solutions on angstrom length scale. This is enabled thanks to the fact that electron scattering is Coulombic in nature, a unique advantage over X-ray and neutron scattering.

## Concept

Measuring ESP distribution with LES is based on a simple physical picture: incident electrons scatter from the sample via Coulombic interaction, therefore a long-ranged ESP

(i.e. large  $\lambda_D$ ) must correspond to a large cross-section, while a short-ranged ESP (i.e. small  $\lambda_D$ ) must correspond to a small cross-section.

The elastic electron scattering cross-section can be expressed as  $I(\mathbf{q}) = |F(\mathbf{q})|^2 = |\mathcal{F}[\phi(\mathbf{r})]|^2$ , where  $\phi(\mathbf{r})$  is the ESP of the sample,  $F(\mathbf{q}) = \mathcal{F}[\phi(\mathbf{r})]$  is the scattering amplitude (a.k.a. form factor),  $\mathcal{F}$  represents the Fourier transform, and  $\mathbf{q}$  is the momentum transfer. **Fig. 1A** show the basic concept of probing ESP distribution with LES. The middle plot shows the simulated electron scattering form factor for a K atom and a  $\text{K}^+$  ion in vacuum. The two form factors are identical for large scattering angle ( $q > 1 \text{ \AA}^{-1}$ ,  $q$ : momentum transfer) but deviates significantly for small scattering angle. In a classical view, large angle scattering events represent electrons that penetrates deep into the electron cloud and scattered by a large ESP from the inner-shell electrons and atomic nuclei. It is the interference of these electrons that form a diffraction pattern which encodes the nuclear structure of matter. Since the inner-shell electron configuration remains the same for the  $\text{K}^+$  ion and the neutral K atom, the large-angle form factors remain identical. On the other hand, small angle scattering events represent electrons that barely penetrate the electron could and scattered by a small ESP from the almost-completely screened nuclei. For cations, one valence electron is lost, the electron could can no longer completely screen the nuclear ESP, and thus the unscreened ESP can fill up the entire space, leading to a diverging form factor at small angle ( $\sim 1/q^2$ ). Quantitatively, this phenomenon can be understood by the Mott-Bethe formula of electron scattering (29, 30), as explained by Eq. S25 in the **Supplementary Materials (SM)**. In the rest of this manuscript, we will refer this method as ESPRESSO—ESP probed with Relativistic Electron Scattering in SOrption.

We developed an LES experimental endstation at the Tsinghua MeV-UED beamline (31), as depicted in **Fig. 1B**. A 1.7 MeV electron beam with a repetition rate of 50 Hz was generated using an rf-type photoinjector. A microfluidic chip was used to generate a free-standing ultrathin liquid sheet in vacuum (32), with a typical width of 400  $\mu\text{m}$  and thickness of 500 nm. To preserve small- $q$  information, the scattering patterns were measured with the main beam directly shone on screen. This method enables the small angle scattering signal to be recorded in full 360° azimuthal angles, which significantly improves the robustness of small angle scattering signal in comparison to previous LES experiments (where only one corner is available) (25). Details about the instrument, experimental process, and data treatment are given in the SM. **Figures 1C-D** present a typical scattering pattern and the angular averaged 1-D scattering intensity, using a 10 mM KCl solution as an example. In each experiment, the scattering intensity for electrolyte solution  $I_{\text{solution}}$  and neat water  $I_{\text{water}}$  was measured separately, and the net scattering intensity from ions are obtained by taking the difference of the two. A background pattern with the main electron beam but without the sample is also measured, displayed as the yellow curve in **Fig. 1D**. The main beam background dominates for  $q < 0.3 \text{ \AA}^{-1}$  and drops to roughly 20% of the total signal at  $q = 0.3 \text{ \AA}^{-1}$  (dashed line). Therefore,  $q < 0.3 \text{ \AA}^{-1}$  was excluded from further analysis in the rest of the manuscript.

Most scattering signals come from solvents. To extract and quantify the scattering signal of solute ions, we define Percentage Difference per Unit Concentration (PDUC) as following:

$$PDUC(q) = \frac{I(q)_{solution} - I(q)_{water}}{I(q)_{water}} * \frac{C_0}{C} \quad (1)$$

where  $C$  is the concentration of electrolyte solution, and  $C_0 = 1000 \text{ mM}$  is the unit concentration. PDUC reports the concentration-normalized scattering cross-section from solute ions.

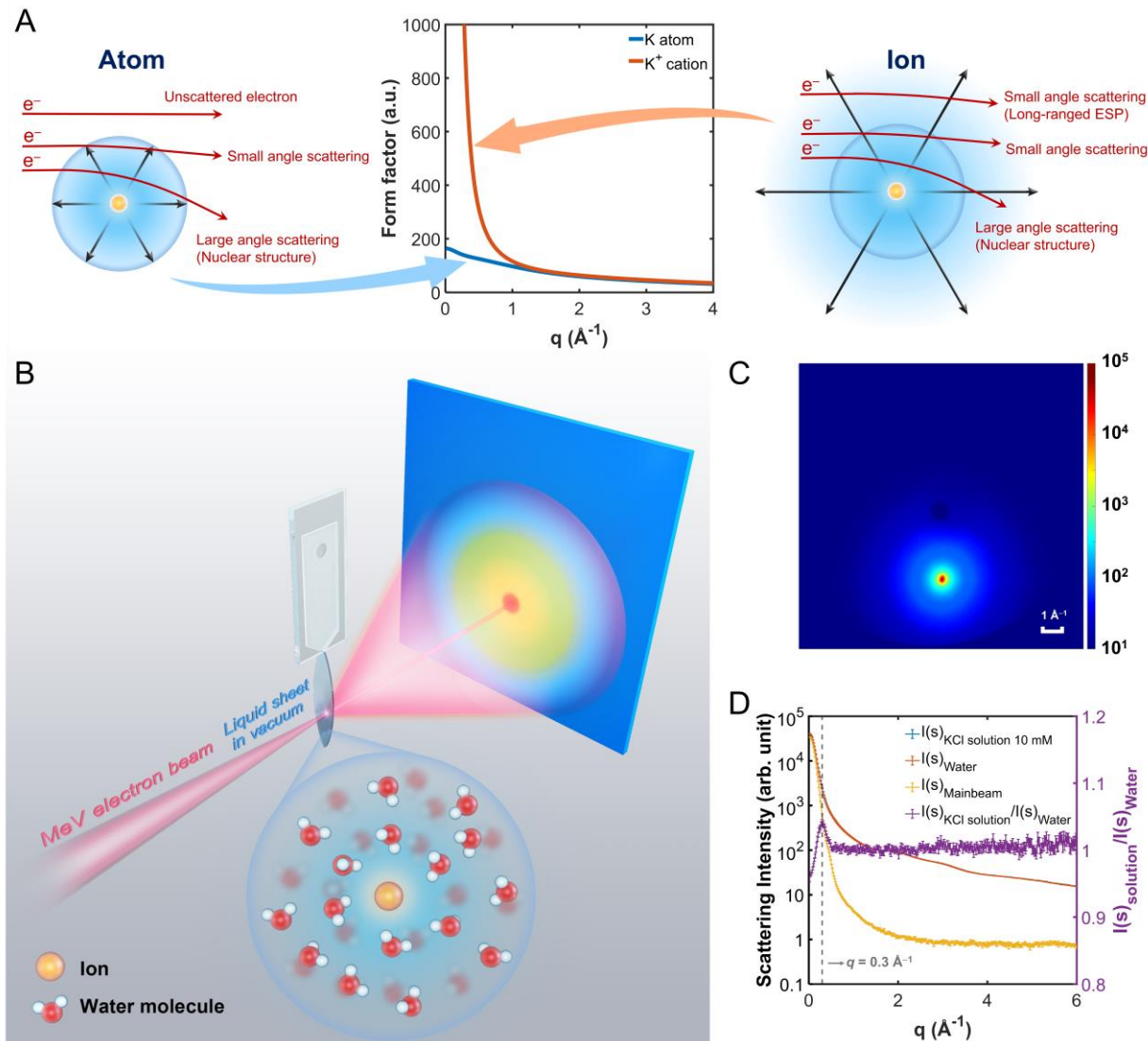


**Fig. 1. Concept and experiment overview.** (A) Form factor plots of K atom and  $K^+$  cation, and conceptual diagrams of electron scattering from an atom (perfectly screened ESP) and a cation (underscreened ESP). (B) Schematic representation of ESPRESSO experiment, an MeV electron beam scatters from an ultrathin liquid electrolyte solution sheet, the scattering pattern and the unscattered main beam are recorded simultaneously on the detector. (C) A typical scattering pattern after baseline removal, in camera counts. (D) Angular averaged scattering intensity of 10 mM KCl solution (blue), pure water

(orange), and main beam background taken without sample (yellow). The intensity ratio between KCl solution and water (purple) is plotted against the right-hand axis. A black dotted line shows  $q = 0.3 \text{ \AA}^{-1}$ , showing a rough separation between the unscattered main beam ( $q < 0.3 \text{ \AA}^{-1}$ ) and the scattering pattern ( $q > 0.3 \text{ \AA}^{-1}$ ). Error bars in D, one S.E.M. of  $\sim 100$  independent measurements.

## Results

**Figure 2A** presents four simulated PDUC curves for KCl solution using the standard LES formula (25):

$$I = \sum_l N_l |f_l(q)|^2 + \sum_{l,m} f_l(q) f_m(q) \frac{N_m (N_l - \delta_{m,l})}{V} 4\pi \int r^2 g_{lm}(r) \frac{\sin(qr)}{qr} dr \quad (2)$$

where the index  $l, m$  represent the atom/ion type,  $N_k$  ( $k = l, m$ ) represents the number of atoms/ions of type  $k$ ,  $f_k$  ( $k = l, m$ ) represents the scattering form factor of atom/ion  $k$ ,  $g_{lm}$  represents the pair distribution function (PDF) of atom pair  $lm$ ,  $\delta_{m,l}$  is the Kronecker delta function, and  $V$  is the volume of the simulated box. The PDFs are simulated using molecular dynamics (MD) simulation with Amoeba 2018 (33) polarizable force field, in a  $25 \text{ \AA} \times 25 \text{ \AA} \times 25 \text{ \AA}$  box that contains  $\sim 500$  water molecules and 1 ion with the periodic boundary condition. The only difference in the three simulated PDUC curves is the scattering form factors for  $\text{K}^+$  and  $\text{Cl}^-$ : blue curve uses atomic form factors, red curve uses unscreened ionic form factors, and yellow and purple curves use partially screened ionic form factors with  $\lambda_D = 5 \text{ \AA}$  and  $20 \text{ \AA}$ , respectively (Detailed in SM). We will refer these models as neutral atom (NA) model, unscreened point charge (UPC) model, and screened point charge (SPC) model in the rest of the manuscript. For large  $q$ , the four curves coincide, showing that they contain the same structural information. For small  $q$ , the four curves differ significantly: PDUC ( $q \rightarrow 0$ ) diverges for UPC model (corresponding to infinite-ranged ESP), drops to nearly zero for NA model (corresponding to short-ranged ESP), and goes in between for SPC model (corresponding to long-ranged ESP). These results reproduce the single-atom scenario (**Fig. 1A**) reasonably well, and demonstrates that ESPRESSO can serve as a sensitive tool for the measurement of ESP distribution around ions.

We measure the PDUC signal experimentally using ESPRESSO, for LiCl, KCl, and KI aqueous solutions with concentrations ranging from 10 to 1000 mM, as shown in **Fig. 2C-H**. For each sample, the PDUC signal at large  $q$  region ( $q > \sim 1 \text{ \AA}^{-1}$ ) are, within the signal-to-noise ratio limit, nearly identical across different concentrations (**Fig. 2 C, E, G**). At small  $q$  region ( $q < \sim 0.5 \text{ \AA}^{-1}$ ), strong concentration-dependent PDUC signals are observed, with PDUC approaching zero at high concentrations while increasing dramatically at low concentrations (**Fig. 2D, F, H**). These results clearly show that ESP around solvated ions is short-ranged & atom-like under high concentration, and long-ranged & ion-like under low concentration.

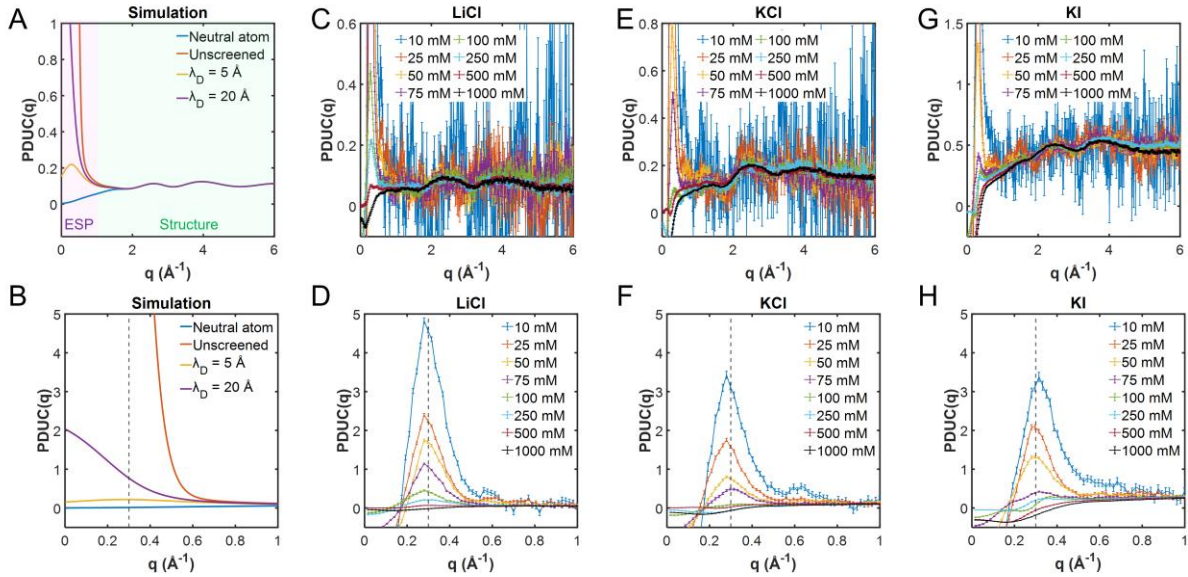


**Fig. 2. Experimental and simulated PDUC results.** (A-B) Simulated PDUC plots for KCl with 4 models: neutral K and Cl atoms (blue), unscreened  $K^+$  and  $Cl^-$  ions (orange), and partially screened  $K^+$  and  $Cl^-$  ions with a Debye length of 5 Å (yellow) and 20 Å (purple), respectively, at large  $q$  range (A) and small  $q$  range (B). All curves are convolved with a Gaussian kernel with  $FWHM = 0.35 \text{ \AA}^{-1}$  to account for the experimental  $q$  resolution. (C to H) Experimental PDUC plots of LiCl across different concentrations at large  $q$  range (C) and small  $q$  range (D). (E to F) and (G to H), similar to (C to D) but for KCl and KI, respectively. Black dotted lines in part (B, D, F, H) locate at  $q = 0.3 \text{ \AA}^{-1}$ , indicating the minimum  $q$  value that can be reliably measured under current experimental conditions. Error bars in C-H, one S.E.M. of 200-1600 independent measurements (Table S2 in SM).

## Debye Length

In electrolyte solution, the Debye screening length  $\lambda_D$  reports the location where the ionic ESP in solution drops to  $1/e$  (or  $\sim 37\%$ ) of that value in-vacuum. To extract  $\lambda_D$  from experimental data, we simulated the PDUC plot with a wide range of  $\lambda_D$ , and found a one-to-one relationship between  $\lambda_D$  value and the slope of the PDUC curve at  $0.4 \text{ \AA}^{-1}$  (Fig. 3A), which is very similar across different types of salt. Using this relationship, we map the experimental PDUC curves to  $\lambda_D$  values, the results are shown in Fig. 3B. For comparison, the  $\lambda_D$  values of DH model for monovalent ions are also displayed. The only assumption in our  $\lambda_D$  retrieval method is that the ESP distribution follows the apparent Debye-Hückel format of  $\frac{\exp(-r/\lambda_D)}{r}$ , no *a-priori* knowledge about the system is used for the retrieval of  $\lambda_D$  values.

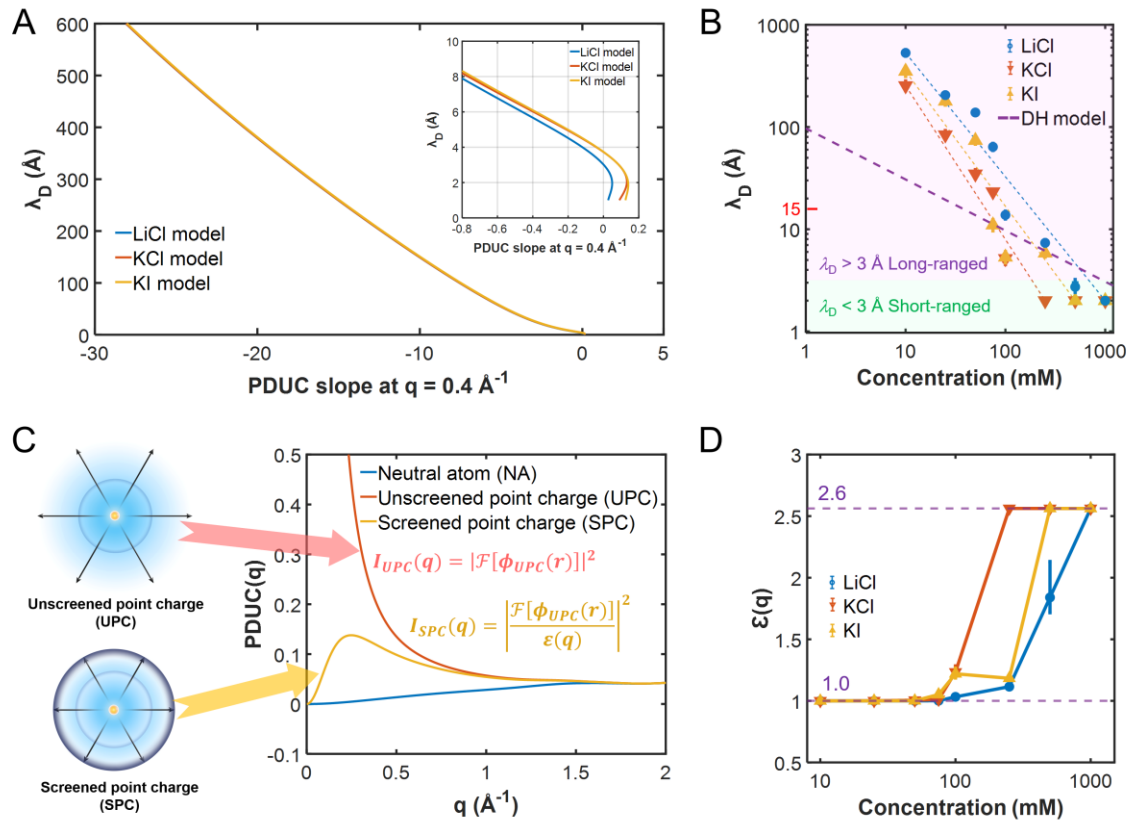


**Fig. 3. Debye length and nonlocal dielectric function.** (A) The relationship between Debye lengths ( $\lambda_D$ ) and PDUC slope values at  $0.4 \text{ \AA}^{-1}$  from simulated LiCl, KCl, and KI model. A one-to-one projection can be established for all three types of salts. The inset figure is a partially enlarged display for the lowest limit of the retrievable  $\lambda_D$  value. (B) Fitted Debye lengths ( $\lambda_D$ ) of LiCl, KCl, and KI at different concentrations, with DH model displayed for comparison. The dashed blue, red and yellow lines serve for eye-guidance, generated by connecting the biggest and the smallest  $\lambda_D$  values (for the same  $\lambda_D$  value, the lowest concentration is chosen) for each sample.  $\lambda_D = 15 \text{ \AA}$  marks the measurement window size under current experimental condition (see text). (C) Concept for the retrieval of NLDF from PDUC curves.  $\mathcal{F}[\phi_{UPC}(r)]$  and  $\mathcal{F}[\phi_{UPC}(r)]/\epsilon(q)$  represents the electron scattering form factor for UPC model and SPC model, respectively. (D) The averaged NLDF value  $\epsilon(q)$  at  $0.4 \text{ \AA}^{-1}$  for LiCl, NaCl, and KI at different concentrations. Dashed lines at  $\epsilon(q) = 1$  and  $\epsilon(q) = 2.6$  marks the lower and the upper limit of current experimental measurement of  $\epsilon(q)$ , respectively. Error bars in B and D, one S.E.M. of 200-1600 independent measurements (Table S2 in SM).

The experimental results of Debye length show a monotonic decrease versus concentration: it starts at hundreds of  $\text{\AA}$  at low concentration, and drops to within the first coordination shell ( $\sim 3 \text{ \AA}$ ) at high concentration. This strong concentration dependence of  $\lambda_D$  clearly shows that the screening primarily originates from counterions rather than solvent environment, reconfirming the fundamental picture of DH model on the microscopic scale (34). Despite its simplicity, the DH model does capture the overall

tendency of Debye length versus concentration. Nevertheless, for all three samples, the change of Debye length against concentration is much faster than that of the DH model. This might originate from the oversimplification of DH model, where it treats both the counterions and the solvent molecules as homogeneous continuum, and neglects the complex behavior such as ion association. This difference does have direct consequences, especially on the question whether ion impact in water is long-ranged or short-ranged. DH model shows that  $\lambda_D$  can go beyond the first solvation shell for any concentration up to  $\sim 1000$  mM, while our experiment suggests that  $\lambda_D$  falls rapidly to within the first solvation shell at a much lower concentration of 200-500 mM. This is to say, for experimental determination of whether ion impact is long-ranged or short-ranged, one needs to be extremely careful with the concentrations used. In fact, in a seminal review, Marcus postulated that the absence of long-ranged effects in ultrafast vibrational spectroscopy experiments could be due to that only high concentration ( $\geq 500$  mM) solutions were studied in these experiments (7). Our  $\lambda_D$  measurements here directly confirm this postulation. Moreover, the proper choice of truncation lengthscale of Coulomb interaction in solution is critical for quantum chemistry calculations in solution phase (35), and our measurement might serve as an experimental benchmark for the rational choice for this lengthscale.

It should be noticed that the experimental  $\lambda_D$  is retrieved using experimental data at  $q = 0.4 \text{ \AA}^{-1}$ , corresponds to a characteristic length scale of  $\frac{2\pi}{0.4} \approx 15 \text{ \AA}$ . For the experimental results of  $\lambda_D \gg 15 \text{ \AA}$  values, rather than the direct measurement of these values, our data should be interpreted as that the ESP barely decays within the 15-Å observation window, and the  $\lambda_D$  is determined by an extrapolation from this window. A direct and more reliable  $\lambda_D$  measurement at longer length scale requires a better experimental  $q$  resolution. On the other hand, the lowest  $\lambda_D$  we can reliably measure is 2 Å (**Fig. 3A** inset), smaller than the first hydration shell radii of all monovalent ions (6).

### Nonlocal dielectric function (NLDF)

The nonlocal dielectric function (NLDF)  $\varepsilon(q)$  serves as a generalized description of the screening behavior of condensed matters, and can be quantum mechanically exact within the framework of linear response theory (36). NLDF takes the whole electrolyte solution as a self-correlated dielectric medium, which is naturally capable of describing the screening behavior from all microscopic contributions, including multipole rearrangement, hydrogen bonding, ion aggregation, and charge density redistribution. The reciprocal-space vector  $q$  shares the same definition with the momentum transfer (i.e. a Fourier transform of the real-space coordinate  $r$ ).  $\varepsilon(q = 0)$  represents the macroscopic dielectric constant while  $\varepsilon(q > 0)$  represents the microscopic dielectric constant at a characteristic length scale of  $2\pi/q$ . The NLDF of neat water has been investigated theoretically and experimentally (37-40). However, the most relevant experimental attempt is based on a classical point-bound-charge electron density model combined with a structural measurement from neutron diffraction (40). This model has at least two disadvantages: 1) it requires the polarization effects in the solvation shells to be accounted separately and explicitly, thus it is not trivial when extending to electrolyte solutions; and 2) it ignores the quantum mechanical many-body interactions in liquid, which is shown to be critical for determining the anomalous macroscopic properties in water (41).

We propose a new method to retrieve NLDF directly from ESPRESSO data, as depicted in **Fig. 3C**. This method is based on the simple physical picture that the elastic electron scattering amplitude is the Fourier transform of the ESP, thus it should scale down by  $\varepsilon(q)$  in comparison to the in-vacuum ionic ESP. The validity of this approach is verified by the successful retrieval  $\varepsilon(q)$  from a mock electron scattering data for DH model with various Debye lengths (**Fig. S10**). Moreover, we would like to point out that the  $\varepsilon(q)$  retrieved by this method accounts for all the quantum mechanical effects, because the incident electron beam interacts with the target sample full quantum mechanically. The only downside for this method is that it can only measure a limited  $q$  range with a maximum  $\varepsilon$  value determined by available experimental  $q$  resolution ( $0.3 < q < 0.5 \text{ \AA}^{-1}$ ,  $\varepsilon_{max} \approx 2.6$  for current experimental condition).

The retrieved  $\varepsilon(q = 0.4 \text{ \AA}^{-1})$  is shown in **Fig. 3D**. The obtained microscopic  $\varepsilon$  values are considerably smaller than the macroscopic bulk dielectric constant of water (80 at 293K), showing completely different screening behaviors on microscopic and macroscopic scales. Theoretical (42, 43) and surface experiment studies (44) support the conclusion that dielectric constant is significantly reduced at microscopic length scales. In addition,  $\varepsilon(q)$  approaches 1 in the low-concentration limit, suggesting that the ionic ESP in dilute electrolyte solutions behave similarly with that in vacuum, at least on the 15-Å observation length scale. This is consistent with the common practice that microscopic interactions between particles are not scaled down by the macroscopic dielectric constant in solution-phase quantum chemistry calculations.

The NLDF plots (**Fig. 3D**) show a critical concentration of around ~100 mM for all three types of salt, where  $\varepsilon(q)$  starts to deviate quickly from 1. This is a typical concentration threshold for the emergence of the specific ion effect (SIE), where many macroscopic physical and chemical properties of electrolyte solution can no longer be explained by classical theory (45). While the root cause of SIE is still far from settled, existing theoretical work does support that SIE is highly related to the ionic ESP distribution (46). The measured  $\varepsilon(q)$  are very close to 1 for concentrations lower than ~100 mM for all types of electrolyte solutions, leading to a similar ESP screening behavior across isovalent ions. This observation might explain the absence of SIE at low concentration. Once the concentration passes the critical value, the  $\varepsilon(q)$  values rise quickly and start to deviate for different ions, with a trend of LiCl < KI < KCl. The association constants ( $K_A$ ) of these three samples have the same trend as  $K_{A,LiCl} < K_{A,KI} < K_{A,KCl}$  (47). A larger  $K_A$  value means more ion-pair formation in the solution, leading to a stronger screening of ESP distribution from counterions, which explains the same trend of their NLDF values and association constants. This trend is also observed in several other macroscopic properties, such as activity coefficient (LiCl > KI > KCl) (48) and conductivity (LiCl < KI < KCl) (49) (**Fig. S16**). To pin down the electrostatic root of SIE would require a comprehensive and systematic study across more types of ions. Nevertheless, NLDF measurements do provide a promising pathway for this task.

In summary, we propose ESPRESSO, an electron-scattering based experimental method that is able to measure both the Debye length and the NLDF in electrolyte solutions. This method extends electron scattering from a structure-probe to an interaction-probe. For all three types of electrolyte solutions studied, the Debye length is always long-ranged for low concentration ( $\leq \sim 100$  mM) and short-ranged for high concentration ( $\geq \sim 500$  mM). The measured Debye lengths are changing over

concentration much faster than the prediction given by the DH model. This finding reconciles with the postulation proposed by Marcus (7), and might settle the 20-year debate over whether the ion impacts on water is long- or short-ranged. Moreover, given that the Debye length underpins a wide range of physical properties in electrolyte solutions and colloids, a direct experimental measurement of Debye length in bulk solution could generate a broad interest across physics, chemistry and biology communities. On the other hand, we show the NLDF  $\varepsilon(q)$  can be retrieved from LES data without relying on complex models or approximations. Since that the NLDF, under the framework of linear response theory, is capable of accounting for the overall screening effects precisely at quantum mechanical level, our method could contribute to a general understanding for the screening effect in solution phase.

## References and Notes

1. H. Ohtaki, T. Radnai, Structure and dynamics of hydrated ions. *Chem. Rev.* **93**, 1157–1204 (1993). doi: [10.1021/cr00019a014](https://doi.org/10.1021/cr00019a014)
2. N. F. A. van der Vegt, K. Haldrup, S. Roke, J. Zheng, M. Lund, H. J. Bakker, Water-mediated ion pairing: Occurrence and relevance. *Chem. Rev.* **116**, 7626–7641 (2016). doi: [10.1021/acs.chemrev.5b00742](https://doi.org/10.1021/acs.chemrev.5b00742)
3. D. T. Bowron, S. D. Moreno, Using synchrotron X-ray and neutron methods to investigate structural aspects of metal ion solvation and solution structure: An approach using empirical potential structure refinement. *Coord. Chem. Rev.* **277**, 2–14 (2014). doi: [10.1016/j.ccr.2014.01.033](https://doi.org/10.1016/j.ccr.2014.01.033)
4. R. Zhang, Z. Pan, W. Zhuang, Modeling the low frequency vibrational spectroscopy of ionic solutions. *Int. J. Quantum Chem.* **115**, 564–569 (2015). doi: [10.1002/qua.24826](https://doi.org/10.1002/qua.24826)
5. C. J. Cramer, D. G. Truhlar, Implicit solvation models: Equilibria, structure, spectra, and dynamics. *Chem. Rev.* **99**, 2161–2200 (1999). doi: [10.1021/cr960149m](https://doi.org/10.1021/cr960149m)
6. Y. Marcus, Ionic-radii in aqueous-solutions. *Chem. Rev.* **88**, 1475–1498 (1988). doi: [10.1021/cr00090a003](https://doi.org/10.1021/cr00090a003)
7. Y. Marcus, Effect of ions on the structure of water: Structure making and breaking. *Chem. Rev.* **109**, 1346–1370 (2009). doi: [10.1021/cr8003828](https://doi.org/10.1021/cr8003828)
8. J. E. Enderby, Ion solvation via neutron scattering. *Chem. Soc. Rev.* **24**, 159–168 (1995). doi: [10.1039/CS9952400159](https://doi.org/10.1039/CS9952400159)
9. P. Debye, E. Hückel, Zur theorie der electrolyte. *Physikalische Zeitschrift* 185–206 (1923).
10. A. M. Smith, A. A. Lee, S. Perkin, The electrostatic screening length in concentrated electrolytes increases with concentration. *J. Phys. Chem. Lett.* **7**, 2157–2163 (2016). doi: [10.1021/acs.jpclett.6b00867](https://doi.org/10.1021/acs.jpclett.6b00867)
11. F. Hofmeister, Zur lehre von der wirkung der salze. *Archiv für experimentelle Pathologie und Pharmakologie* **24**, 247–260 (1888). doi: [10.1007/BF01918191](https://doi.org/10.1007/BF01918191)
12. R. Leberman, A. K. Soper, Effect of high-salt concentrations on water-structure. *Nature* **378**, 364–366 (1995). doi: [10.1038/378364a0](https://doi.org/10.1038/378364a0)
13. R. Mancinelli, A. Botti, F. Bruni, M. A. Ricci, A. K. Soper, Perturbation of water structure due to monovalent ions in solution. *Phys. Chem. Chem. Phys.* **9**, 2959–2967 (2007). doi: [10.1039/B701855J](https://doi.org/10.1039/B701855J)
14. R. Buchner, T. Chen, G. Hefter, Complexity in “simple” electrolyte solutions: Ion pairing in  $\text{MgSO}_4$ (aq). *J. Phys. Chem. B* **108**, 2365–2375 (2004). doi: [10.1021/jp034870p](https://doi.org/10.1021/jp034870p)
15. W. Wachter, Š. Fernandez, R. Buchner, G. Hefter, Ion association and hydration in aqueous solutions of  $\text{LiCl}$  and  $\text{Li}_2\text{SO}_4$  by dielectric spectroscopy. *J. Phys. Chem. B* **111**, 9010–9017 (2007). doi: [10.1021/jp072425e](https://doi.org/10.1021/jp072425e)
16. M. F. Kropman, H. J. Bakker, Vibrational relaxation of liquid water in ionic solvation shells. *Chem. Phys. Lett.* **370**, 741–746 (2003). doi: [10.1016/S0009-2614\(03\)00123-4](https://doi.org/10.1016/S0009-2614(03)00123-4)

17. A. W. Omta, M. F. Kropman, S. Woutersen, H. J. Bakker, Negligible effect of ions on the hydrogen-bond structure in liquid water. *Science* **301**, 347–349 (2003). doi: [10.1126/science.1084801](https://doi.org/10.1126/science.1084801)
18. K. J. Tielrooij, N. Garcia-Araez, M. Bonn, H. J. Bakker, Cooperativity in ion hydration. *Science* **328**, 1006–1009 (2010). doi: [10.1126/science.1183512](https://doi.org/10.1126/science.1183512)
19. G. Stirnemann, E. Wernersson, P. Jungwirth, D. Laage, Mechanisms of acceleration and retardation of water dynamics by ions. *J. Am. Chem. Soc.* **135**, 11824–11831 (2013). doi: [10.1021/ja405201s](https://doi.org/10.1021/ja405201s)
20. K. Hpone Myint, W. Ding, A. P. Willard, The influence of spectator cations on solvent reorganization energy is a short-range effect. *J. Phys. Chem. B* **125**, 1429–1438 (2021). doi: [10.1021/acs.jpcb.0c09895](https://doi.org/10.1021/acs.jpcb.0c09895)
21. C. Zhang, S. Yue, A. Z. Panagiotopoulos, M. L. Klein, X. Wu, Dissolving salt is not equivalent to applying a pressure on water. *Nat. Commun.* **13**, 822 (2022). doi: [10.1038/s41467-022-28538-8](https://doi.org/10.1038/s41467-022-28538-8)
22. J. T. O'Brien, J. S. Prell, M. F. Bush, E. R. Williams, Sulfate ion patterns water at long distance. *J. Am. Chem. Soc.* **132**, 8248–8249 (2010). doi: [10.1021/ja1024113](https://doi.org/10.1021/ja1024113)
23. J. Duboisset, P.-F. Brevet, Salt-induced long-to-short range orientational transition in water. *Phys. Rev. Lett.* **120**, 263001 (2018). doi: [10.1103/PhysRevLett.120.263001](https://doi.org/10.1103/PhysRevLett.120.263001)
24. Y. Chen, H. I. Okur, N. Gomopoulos, C. Macias-Romero, P. S. Cremer, P. B. Petersen, G. Tocci, D. M. Wilkins, C. Liang, M. Ceriotti, S. Roke, Electrolytes induce long-range orientational order and free energy changes in the h-bond network of bulk water. *Sci. Adv.* **2**, e1501891 (2016). doi: [10.1126/sciadv.1501891](https://doi.org/10.1126/sciadv.1501891)
25. J. P. F. Nunes, K. Ledbetter, M. Lin, M. Kozina, D. P. DePonte, E. Biasin, M. Centurion, C. J. Crissman, M. Dunning, S. Guillet, K. Jobe, Y. Liu, M. Mo, X. Shen, R. Sublett, S. Weathersby, C. Yoneda, T. J. A. Wolf, J. Yang, A. A. Cordones, X. J. Wang, Liquid-phase mega-electron-volt ultrafast electron diffraction. *Struct. Dyn.* **7**, 024301 (2020). doi: [10.1063/1.5144518](https://doi.org/10.1063/1.5144518)
26. J. D. Koralek, J. B. Kim, P. Bruza, C. B. Curry, Z. Chen, H. A. Bechtel, A. A. Cordones, P. Sperling, S. Toleikis, J. F. Kern, S. P. Moeller, S. H. Glenzer, D. P. DePonte, Generation and characterization of ultrathin free-flowing liquid sheets. *Nat. Commun.* **9**, 1353 (2018). doi: [10.1038/s41467-018-03696-w](https://doi.org/10.1038/s41467-018-03696-w)
27. J. Yang, J. P. F. Nunes, K. Ledbetter, E. Biasin, M. Centurion, Z. Chen, A. A. Cordones, C. Crissman, D. P. DePonte, S. H. Glenzer, M. F. Lin, M. Mo, C. D. Rankine, X. Shen, T. J. A. Wolf, X. Wang, Structure retrieval in liquid-phase electron scattering. *Phys. Chem. Chem. Phys.* **23**, 1308–1316 (2021). doi: [10.1039/d0cp06045c](https://doi.org/10.1039/d0cp06045c)
28. J. Yang, R. Dettori, J. P. F. Nunes, N. H. List, E. Biasin, M. Centurion, Z. Chen, A. A. Cordones, D. P. DePonte, T. F. Heinz, M. E. Kozina, K. Ledbetter, M. F. Lin, A. M. Lindenberg, M. Mo, A. Nilsson, X. Shen, T. J. A. Wolf, D. Donadio, K. J. Gaffney, T. J. Martinez, X. Wang, Direct observation of ultrafast hydrogen bond strengthening in liquid water. *Nature* **596**, 531–535 (2021). doi: [10.1038/s41586-021-03793-9](https://doi.org/10.1038/s41586-021-03793-9)
29. N. F. Mott, The scattering of electrons by atoms. *Proc. R. Soc. Lond. A* **127**, 658–665 (1930). doi: [10.1098/rspa.1930.0082](https://doi.org/10.1098/rspa.1930.0082)
30. H. Bethe, On the theory of the passage of rapid charged particle radiation through matter. *Annalen Der Physik* **5**, 325–400 (1930).
31. R. Li, W. Huang, Y. Du, L. Yan, Q. Du, J. Shi, J. Hua, H. Chen, T. Du, H. Xu, C. Tang, Note: Single-shot continuously time-resolved mev ultrafast electron diffraction. *Rev. Sci. Instrum.* **81**, 036110 (2010). doi: [10.1063/1.3361196](https://doi.org/10.1063/1.3361196)
32. C. J. Crissman, M. Mo, Z. Chen, J. Yang, D. A. Huyke, S. H. Glenzer, K. Ledbetter, J. P. F. Nunes, M. L. Ng, H. Wang, X. Shen, X. Wang, D. P. DePonte, Sub-micron thick liquid sheets produced by isotropically etched glass nozzles. *Lab Chip* **22**, 1365–1373 (2022). doi: [10.1039/D1LC00757B](https://doi.org/10.1039/D1LC00757B)
33. C. Zhang et al., AMOEBA Polarizable Atomic Multipole Force Field for Nucleic Acids. *Chem. Theory Comput.* **14**, 2084–2108 (2018). Doi: [10.1021/acs.jctc.7b01169](https://doi.org/10.1021/acs.jctc.7b01169)
34. M. Costa Reis, Ion activity models: The debye-hückel equation and its extensions. *ChemTexts* **7**, 9 (2021). doi: [10.1007/s40828-020-00130-x](https://doi.org/10.1007/s40828-020-00130-x)
35. A. Gao, R. C. Remsing, J. D. Weeks, Short solvent model for ion correlations and hydrophobic association. *Proc. Natl. Acad. Sci. U.S.A.* **117**, 1293–1302 (2020). doi: [10.1073/pnas.1918981117](https://doi.org/10.1073/pnas.1918981117)

36. R. Kubo, The fluctuation-dissipation theorem. *Rep. Prog. Phys.* **29**, 255 (1966). doi: [10.1088/0034-4885/29/1/306](https://doi.org/10.1088/0034-4885/29/1/306)

37. A. A. Kornyshev, Nonlocal screening of ions in a structurized polar liquid — new aspects of solvent description in electrolyte theory. *Electrochim. Acta* **26**, 1–20 (1981). doi: [10.1016/0013-4686\(81\)80001-1](https://doi.org/10.1016/0013-4686(81)80001-1)

38. A. A. Kornyshev, S. Leikin, G. Sutmann, “Overscreening” in a polar liquid as a result of coupling between polarization and density fluctuations. *Electrochim. Acta* **42**, 849–865 (1997). doi: [10.1016/S0013-4686\(96\)00330-1](https://doi.org/10.1016/S0013-4686(96)00330-1)

39. F. O. Raineri, H. Resat, H. L. Friedman, Static longitudinal dielectric function of model molecular fluids. *J. Chem. Phys.* **96**, 3068–3084 (1992). doi: [10.1063/1.46195](https://doi.org/10.1063/1.46195)

40. P. A. Bopp, A. A. Kornyshev, G. Sutmann, Static nonlocal dielectric function of liquid water. *Phys. Rev. Lett.* **76**, 1280–1283 (1996). doi: [10.1103/PhysRevLett.76.1280](https://doi.org/10.1103/PhysRevLett.76.1280)

41. T. Morawietz, A. Singraber, C. Dellago, J. Behler, How van der waals interactions determine the unique properties of water. *Proc. Natl. Acad. Sci. U.S.A.* **113**, 8368–8373 (2016). doi: [10.1073/pnas.1602375113](https://doi.org/10.1073/pnas.1602375113)

42. J. Mazur, R. L. Jernigan, Distance-dependent dielectric constants and their application to double-helical DNA. *Biopolymer* **31**, 1615–1629 (1991). doi: [10.1002/bip.360311316](https://doi.org/10.1002/bip.360311316)

43. C. Schaaf, S. Gekle, Dielectric response of the water hydration layer around spherical solutes. *Phys. Rev. E* **92**, 032718 (2015). doi: [10.1103/PhysRevE.92.032718](https://doi.org/10.1103/PhysRevE.92.032718)

44. O. Teschke, G. Ceotto, E. F. de Souza, Interfacial water dielectric-permittivity-profile measurements using atomic force microscopy. *Phys. Rev. E* **64**, 011605 (2001). doi: [10.1103/PhysRevE.64.011605](https://doi.org/10.1103/PhysRevE.64.011605)

45. P. Lo Nostro, B. W. Ninham, Hofmeister phenomena: An update on ion specificity in biology. *Chem. Rev.* **112**, 2286–2322 (2012). doi: [10.1021/cr200271j](https://doi.org/10.1021/cr200271j)

46. K. P. Gregory, E. J. Wanless, G. B. Webber, V. S. J. Craig, A. J. Page, The electrostatic origins of specific ion effects: Quantifying the hofmeister series for anions. *Chem. Sci.* **12**, 15007–15015 (2021). doi: [10.1039/DSC03568A](https://doi.org/10.1039/DSC03568A)

47. J. Gujt, M. Bešter-Rogač, B. Hribar-Lee, An investigation of ion-pairing of alkali metal halides in aqueous solutions using the electrical conductivity and the monte carlo computer simulation methods. *J. Mol. Liq.* **190**, 34–41 (2014). doi: [10.1016/j.molliq.2013.09.025](https://doi.org/10.1016/j.molliq.2013.09.025)

48. W. J. Hamer, Y. C. Wu, Osmotic coefficients and mean activity coefficients of uni-univalent electrolytes in water at 25°C. *J. Phys. Chem. Ref. Data* **1**, 1047–1100 (2009). doi: [10.1063/1.3253108](https://doi.org/10.1063/1.3253108)

49. D. E. Goldsack, R. Franchetto, A. Franchetto, Solvation effects on the conductivity of concentrated electrolyte solutions. *Can. J. Chem.* **54**, 2953–2966 (1976). doi: [10.1139/v76-418](https://doi.org/10.1139/v76-418)

50. F. Salvat, A. Jablonski, C. J. Powell, Elsepa—dirac partial-wave calculation of elastic scattering of electrons and positrons by atoms, positive ions and molecules. *Comp. Phys. Commun.* **165**, 157–190 (2005). doi: [10.1016/j.cpc.2004.09.006](https://doi.org/10.1016/j.cpc.2004.09.006)

51. M. E. Tuckerman, B. J. Berne, G. J. Martyna, Molecular dynamics algorithm for multiple time scales: Systems with long range forces. *J. Chem. Phys.* **94**, 6811–6815 (1991). doi: [10.1063/1.460259](https://doi.org/10.1063/1.460259)

52. G. Bussi, D. Donadio, M. Parrinello, Canonical sampling through velocity rescaling. *The J. Chem. Phys.* **126**, 014101 (2007). doi: [10.1063/1.2408420](https://doi.org/10.1063/1.2408420)

53. U. Essmann, L. Perera, M. L. Berkowitz, T. Darden, H. Lee, L. G. Pedersen, A smooth particle mesh ewald method. *J. Chem. Phys.* **103**, 8577–8593 (1995). doi: [10.1063/1.470117](https://doi.org/10.1063/1.470117)

54. S. Miyamoto, P. A. Kollman, Settle: An analytical version of the shake and rattle algorithm for rigid water models. *J. Comput. Chem.* **13**, 952–962 (1992). doi: [10.1002/jcc.540130805](https://doi.org/10.1002/jcc.540130805)

55. J. A. Rackers, Z. Wang, C. Lu, M. L. Laury, L. Lagardère, M. J. Schnieders, J. P. Piquemal, P. Ren, J. W. Ponder, Tinker 8: Software tools for molecular design. *J. Chem. Theory Comput.* **14**, 5273–5289 (2018). doi: [10.1021/acs.jctc.8b00529](https://doi.org/10.1021/acs.jctc.8b00529)

56. M. Centurion, T. J. A. Wolf, J. Yang, Ultrafast imaging of molecules with electron diffraction. *Annu. Rev. Phys. Chem.* **73**, 21–42 (2022). doi: [10.1146/annurev-physchem-082720-010539](https://doi.org/10.1146/annurev-physchem-082720-010539)

57. J. H. Hubbell, W. J. Veigle, E. A. Briggs, R. T. Brown, D. T. Cromer, R. J. Howerton, Atomic form factors, incoherent scattering functions, and photon scattering cross sections. *J. Phys. Chem. Ref. Data* **4**, 471–538 (1975). doi: [10.1063/1.555523](https://doi.org/10.1063/1.555523)

58. R. Srinivasan, V. A. Lobastov, C. Y. Ruan, A. H. Zewail, Ultrafast electron diffraction (UED): A new development for the 4D determination of transient molecular structures. *Helv. Chim. Acta* **86**, 1761–1799 (2003). doi: [10.1002/hlca.200390147](https://doi.org/10.1002/hlca.200390147)
59. The Engineering ToolBox (2004). Evaporation from a Water Surface. [online] Available at: [https://www.engineeringtoolbox.com/evaporation-water-surface-d\\_690.html](https://www.engineeringtoolbox.com/evaporation-water-surface-d_690.html)
60. J. Wang, A. N. Tripathi, V. H. Smith, Jr., Chemical binding and electron correlation effects in X-ray and high energy electron scattering. *J. Chem. Phys.* **101**, 4842–4854 (1994). doi: [10.1063/1.467407](https://doi.org/10.1063/1.467407)

### **Acknowledgments:**

We acknowledge the help from Qiong Wu, Yijiang Zhu, and Xingwei Guo for experimental assistance. We acknowledge helpful discussions with Zhonghan Hu and Steve Boxer.

### **Funding:**

National Key Research and Development Program of China 2021YFA1601200 (B.H., Y.N.Y., R.N.H., K.K.C., Z.Y.W., L.T.Y, Y.A.W, H.W.C., Y.X.H., P.L., H.R.M, Y.M.T, L.M.Z., L.H.L., J.Y.)

National Natural Science Foundation of China 22273044 (B.H., K.K.C., L.T.Y, H.W.C, H.R.M, J.Y.)

Tsinghua University Initiative Scientific Research Program 20197050028 (Y.N.Y., Z.Y.W., Y.A.W., Y.C.D., P.L., Y.M.T., R.K.L.)

### **Author contributions:**

Conceptualization: J.Y.

Supervision: R.K.L. and J.Y.

Resources: B.H., Y.C.D., P.J.J., L.M.Z., L.H.L., R.K.L., and J.Y.

Experimental methodology: B.H., Y.N.Y., H.W.C., R.K.L., J.Y.

Experimental data curation: B.H., Y.N.Y., K.K.C., L.T.Y, Z.Y.W., Y.A.W, P.L., Y.M.T.

Experimental data analysis and interpretation: K.K.C., B.H., J.Y.

MD simulation: R.N.H., Y.X.H., L.H.L.

Visualization: B.H., K.K.C., L.T.Y., and J.Y.

Funding acquisition: L.H.L., R.K.L., and J.Y.

Project administration: R.K.L. and J.Y.

Writing – original draft: B.H., K.K.C., and J.Y.

Writing – review & editing: B.H., K.K.C., L.H.L., R.K.L., and J.Y.

**Competing interests:** Authors declare that they have no competing interests.



# Supplementary Material

## Materials and Methods

### Chemical materials

All solute samples used in this work, including LiCl (Analytical Reagent, 99.0%), KCl (Analytical Reagent, 99.5%), and KI (Analytical Reagent, 99.0%), were commercially purchased from Macklin Biochemical Technology Co., Lt., without further purification. Standard caffeine solution was provided by Sichuan Zhongce RM Co., Lt., product No. BWY0820059. Deionized water was produced from Molgy60d water purifier (Molecular Technology Co., Lt.).

### Preparation of electrolyte solutions

Samples at concentrations of 10, 25, 50, 75, 100, 250, 500, and 1000 mM were prepared for the LES experiment. The solutions were precisely prepared using volumetric flasks with high precision to ensure the accurate concentrations.

### Liquid electron scattering (LES) endstation

We developed an LES experimental endstation at the Tsinghua MeV-UED beamline, with electron gun, collimation system, liquid sample chamber & in-vacuum liquid sheet system, vacuum system, and scattering detector system. Details are given in the following paragraphs.

*Electron beam source and collimation system.* As shown in **Fig. S1A**, a photocathode RF electron gun was used to produce high brightness electron beam. The FWHM pulse duration of the 266 nm driving laser (for electron beam generation) is 150 fs. After extraction, we used a 40 MV/m high gradient 1.6-cell S-band rf gun to accelerate the electrons to 1.7 MeV in order to preserve high beam quality from space charge effects. The machine is operated under 50 Hz repetition rate. The electron beam was focused by two focusing solenoids and steered with four two-dimension steering magnets. Two thick bronze apertures installed on two-dimension linear translation stages were used to shape beam size, whose diameters is 0.1 mm (upstream) and 0.3 mm (downstream), respectively. The spot size of the electron beam on the liquid sheet is 150  $\mu$ m FWHM in horizontal and 250  $\mu$ m FWHM in vertical direction, with  $10^4$ – $10^5$  electrons per pulse.

*Liquid sample chamber & sample delivery system.* The chamber design is similar to the SLAC LUED sample chamber (25). The liquid sample was pumped into the chamber by a HPLC pump (20ADX, Shimazu Ltd.) with low pressure gradient valve (LPGE UNIT20A, Shimazu Ltd.) and a degasser device (DGU-20A<sub>3</sub>R, Shimazu Ltd.). The liquid sheet (as shown in **Fig. S1B**) was produced by the commercial micro-fluidic chip (Micronit) with a 4 mL/min flow velocity, and was captured with a commercial jet catcher (iRS jet catcher system spare Catcher Tips with ~400  $\mu$ m orifice diameter, Innovative Research Solutions GmbH) after the interaction region. The liquid sample was then collected by a collection bottle in a cold trap (CT4-50, Coolium Instruments Ltd.) outside the chamber. The whole liquid sheet setup was mounted on a 2-D stage assembly and the microfluidic chip was mounted on a 3-D stage assembly (MFA-CCV6, Newport Co. Ltd. and No.6230V62000, PI Ltd.).

*Liquid sheet.* The liquid sheet used in each experiment was generated with the same parameters. **Fig. S2** shows the liquid sheets of pure water and KI solutions at different concentrations (atmosphere condition), there is no obvious difference of interferometric fringe for different concentrations. With the same flow velocity of 4 mL/min, the length of liquid sheet in vacuum is ~3 mm and the width is ~400  $\mu$ m. In the scattering experiment, the interaction point is ~700  $\mu$ m from the bottom of the first liquid sheet. The thickness of the sheet is ~500 nm.

*Vacuum system.* A multistage differential vacuum system was implemented to protect the electron gun from liquid vapor. Five turbo pumps (three TwisTorr 74FS CFF2.75, Agilent Ltd. and two CXF1401, KYKY Technology Ltd.) were used to maintain the vacuum level during LES experiment. A typical vacuum reading during an LES experiment is 3e-3 torr at sample chamber, 3e-6 torr at 1<sup>st</sup> upstream differential stage, 1e-6 torr at 2<sup>nd</sup> upstream differential stage, and 3e-4 torr at downstream. To handle the water vapor, a screw pump (NSP20, Zhejiang VALUE Mechanical & Electrical Products Ltd.) was used as the backing pump for the KYKY turbo pumps.

*Scattering detector system.* The detector was comprised of a phosphor screen with a central hole (2 mm diameter), a 45-degree mirror with a central hole (1.8 mm diameter) and an EMCCD camera.

### Experimental data collection

For each experimental condition, scattering data for neat water and electrolyte solution was collected repeatedly with a scheme of water–solution–water–solution–water–solution..., with 5-minute acquisition time before each switch. The first 30 seconds of data after each switch was discarded to ensure the sample purity. This delay time was determined by a real-time UV-Vis spectroscopy measurement of caffeine (as shown in **Fig. S3**). Two background patterns, one without sample and the other without electron beam, were collected for each experimental condition. All scattering data were collected with an exposure time of 1 second and an EM gain setting between 40 and 60.

### Scattering data treatment

The raw 2-D patterns are treated with a standard clean-up procedure, including pattern background removal, gain-map calibration, masking the pattern, electron main beam fitting, data selection, azimuthal averaging, and the water–solution calibration. Details are given in the following paragraphs.

#### 1. *Pattern background removal*

The background patterns without electron beam are collected with the same gain and exposure. A typical image of scattering pattern and the background are shown in **Fig. S4**. The corresponding background removal result is shown in **Fig. S5**.

For each scattering pattern  $A_{raw}$  (**Fig. S5A**), the background is removed as follows:

$$A_{bkg_{removed}} = A_{raw} - k \frac{BL_{A_{raw}}}{BL_{M_{bkg}}} M_{bkg}. \quad (\text{Eq. S1})$$

Here,  $M_{bkg}$  is the median pattern of all collected background patterns,  $BL_{A_{raw}}$  and  $BL_{M_{bkg}}$  are the baseline values of  $A_{raw}$  and  $M_{bkg}$ , and  $k$  is a scaling parameter of  $M_{bkg}$ . The baseline value is determined by taking the median value of the four 100\*100 corners of each scattering pattern (**Fig. S5A**), which scales the self-fluctuation of EMCCD background. Define the residue of the background patterns as:

$$res = \sum_i \text{mean} \left( B_i - k \frac{C_{B_i}}{C_{M_{bkg}}} M_{bkg} \right). \quad (\text{Eq. S2})$$

Here,  $B_i$  is the  $i^{th}$  background pattern and operator  $\text{mean}(\cdot)$  represents getting the mean value of the counts of all pixels in the 2-D pattern. The scaling parameter  $k$  is determined by setting the residue  $res = 0$ , which means that the background patterns should be exactly removed by themselves. **Fig. S5A-B** shows the scattering pattern before and after background removal treatment.

## 2. Gain-map calibration

The intensity of pixels close to the hole on the phosphor screen is reduced systematically due to the hole in the 45-degree mirror. We measured a gain-map by scanning the electron beam on the detector (**Fig. S5E**). The pixel count within 120 pixels from the center of the hole is compensated by the gain-map. A typical pattern after gain-map calibration is shown in **Fig. S5C**. This operation does not influence the small-angle scattering signal around the electron beam.

## 3. Masking the pattern

To remove several obvious detector artifacts, a mask treatment is applied to the pattern, as shown in **Fig. S5D**.

## 4. Electron main beam fitting

Each single scattering pattern, containing the unscattered electron beam (**Fig. S6A**) and the scattering signal, is fitted by the following superposition of two 2-D gaussian function (with 9 parameters:  $x_c, y_c, \theta, f_x, f_y, f, a_1, a_2, c$ ), one accounts for the main beam and the other accounts for the scattering signal:

$$g(x, y) = a_1 \exp \left( -4 \log(2) \left( \frac{X^2}{f_x^2} + \frac{Y^2}{f_y^2} \right) \right) + a_2 \exp \left( -4 \log(2) \left( \frac{(x - x_c)^2}{f^2} + \frac{(y - y_c)^2}{f^2} \right) \right) + c, \quad (\text{Eq. S3})$$

$$X = (x - x_c) \cos(\theta) - (y - y_c) \sin(\theta), \quad (\text{Eq. S4})$$

$$Y = (x - x_c) \sin(\theta) + (y - y_c) \cos(\theta). \quad (\text{Eq. S5})$$

Here,  $x$  and  $y$  are the coordinates of the scattering pattern,  $(x_c, y_c)$  is the center position of the unscattered electron beam and the scattering signal,  $\theta$  is the orientational angle of the unscattered electron beam,  $f_x$  and  $f_y$  are the FWHMs of the unscattered electron beam,  $f$  is the FWHM of the fitted Gaussian function of scattering signal,  $a_1$  and  $a_2$ , represent the amplitude of the two Gaussian function, and  $c$  is the offset constant. The parameters are depicted in **Fig. S6B**. The fitting function naturally describes the position, size, amplitude and orientation of the electron beam, and the center, size and amplitude

of the diffraction signal. Note that the center of the scattering signal should be exactly the same as the position of the electron beam. The fitting results of electron beam and scattering pattern are shown in **Fig. S6C-D**.

### 5. Scattering data selection

The condition of each scattering pattern, affected by the fluctuation of electron beam, sample delivery and other experimental conditions, is evaluated by the following 11 parameters: the 8 parameters in the electron beam fitting ( $x_c, y_c, \theta, f_x, f_y, f, a_1, a_2$ ), the  $\chi^2$  value of fitting, total count value within the normalization ring (discussed in section 7), and the ratio of electron beam amplitude over the total count value. Scattering pattern with any of these parameters deviating more than 1.5 times the standard deviation away from the median is removed from further treatment. Around 30% of the data are removed in this process.

### 6. Azimuthal averaging

2-D patterns are converted to 1-D intensities by azimuthal averaging, with the center ( $x_c, y_c$ ) determined from the electron beam fitting. Discrete radial step is set to 1 pixel ( $0.0175 \text{ \AA}^{-1}$ ) and  $q$  maximum is set to  $12 \text{ \AA}^{-1}$ . At each radial distance, pixels that are more than 3 times the standard deviation from the median are removed. The numbers of final obtained scattering data are listed in **Table S1**.

### 7. Water-solution balance

The scattering patterns of neat water and electrolyte solutions are not directly comparable, because the liquid sheets of the water and electrolyte solution may have different thickness. We balance the water and solution scattering by two steps: 1) Normalize the two diffraction patterns using the total camera counts between  $1.5$  and  $3.3 \text{ \AA}^{-1}$  (within the normalization ring shown in **Fig. S4F**). This region was chosen because the scattering signal here is dominated by elastic scattering with a good SNR. The total count normalization also removes any other linear change of scattering intensity. 2) Multiply a water-solution balance coefficient to the solution scattering intensity. This is because in electrolyte solution, the scattering signal comes from both the solute and the solvent, which is supposed to be stronger than the neat water. This coefficient balances the water concentration between neat water and solvent water.

We use the solute concentration and the elastic scattering cross section under IAM to estimate this coefficient. A complete list of water-solution balance coefficient is given in **Table S2**. This coefficient is very close to 1 for most cases, but can be as large as 1.45 for 1000 mM KI, where both the concentration and the atomic number of solute ions are high. The detailed method on how to calculate this coefficient is described in the following paragraphs.

Define the molar ratio ( $n_{ws}$ ) of water to salt in the electrolyte solution with concentration  $C_s$  (in unit mM) as:

$$n_{ws}(C_s) = \frac{C_w}{C_s}. \quad (\text{Eq. S6})$$

Here,  $C_w$  is the concentration of water (in unit mM). The water-solution balance coefficient  $k_{ws}$  is:

$$k_{ws} = \frac{n_{ws}\sigma_w + \sigma_s}{n_{ws}\sigma_w}. \quad (\text{Eq. S7})$$

Here,  $\sigma$  represents the elastic cross section ( $\sigma_s = \sigma_{cation} + \sigma_{anion}$  and  $\sigma_w = \sigma_O + 2\sigma_H$ ). The coefficient describes the elastic scattering ratio of the solution to water, so that

the water concentration between neat water and solvent water is balanced. The cross sections of ions are approximated by that of corresponding atoms, which is a good approximation between 1.5 and 3.3 Å<sup>-1</sup>. The elastic cross sections of atoms are taken from ELSEPA (50). The water-salt  $n_{ws}$  ratios of LiCl, KCl, and KI at different concentrations are obtained by a linear extrapolation from a measured  $n_{ws}$  ratio at concentration of 500 mM (109.41 for LiCl, 108.68 for KCl, and 108.15 for KI) using the following equation,

$$n_{ws}(C_s) = n_{ws}(C_s = 500 \text{ mM}) \frac{500}{C_s}. \quad (\text{Eq. S8})$$

To check the accuracy of the extrapolation, we explicitly measured the  $n_{ws}$  for each concentration of KI solution, and used both sets of  $k_{ws}$  in the following data analysis. The two methods have a negligible overall difference (<0.007 in PDUC), as shown in **Fig. S7B-C**.

To further verify the water-solution balance method, **Fig. S7** shows the PDUC curves of 1000 mM and 100 mM KI solutions, with different water-solution balance coefficients applied. Without this coefficient, the large-angle PDUC approaches zero while the PDUC( $q < 2 \text{ \AA}^{-1}$ ) goes negative, which is unphysical because the net difference introduced by the solute should be positive (**Fig. S7A**). With this coefficient, the large-angle PDUC for both concentrations match with each other (indicating the identical structure with concentration normalized), and the PDUC( $q < 2 \text{ \AA}^{-1}$ ) becomes positive (**Fig. S7B**).

### Simulation method

#### 1. Independent Atom Model (IAM) simulation

The scattering intensity under the IAM of liquid water is simulated by:

$$I_{w,at}(q) = N_w (|f_O(q)|^2 + 2|f_H(q)|^2 + S_O(q)), \quad (\text{Eq. S9})$$

$$I_{w,mol}(q) = \sum_{m,n} f_m(q) f_n(q) \frac{N_m(N_n - \delta_{mn})}{L^3} \int_0^L r^2 dr \frac{\sin(qr)}{qr} (g_{m,n}(r) - 1), \quad (\text{Eq. S10})$$

$$I_{w,sim}(q) = I_{w,at}(q) + I_{w,mol}(q). \quad (\text{Eq. S11})$$

Here,  $N_w$  is the number of water molecules in the simulated molecular dynamics simulation (MD) box,  $L$  is the side-length of the box,  $f_O(q)$  and  $f_H(q)$  are the form factors of O and H atom,  $S_O(q)$  is the inelastic form factor of O atom, subscript  $m$  and  $n$  represent atomic types in water (O or H), and  $g_{m,n}(r)$  is the radial distribution function (RDF) of the two types of atoms. The scattering intensity of electrolyte solution is simulated by:

$$I_{ion,at}(q) = \frac{N_w}{n_{ws}} (|f_{cat}(q)|^2 + |f_{ani}(q)|^2), \quad (\text{Eq. S12})$$

$$I_{ion,mol}(q) = \sum_{i,n} f_i(q) f_n(q) \frac{N_w N_n}{n_{ws} L^3} \int_0^L r^2 dr \frac{\sin(qr)}{qr} (g_{i,n}(r) - 1), \quad (\text{Eq. S13})$$

$$I_{s,sim}(q) = I_{w,sim}(q) + I_{ion,at}(q) + I_{ion,mol}(q). \quad (\text{Eq. S14})$$

Here, the subscript  $i$  represents all types of ions (cations and anions). The RDFs used for simulation in Eq. S10 and Eq. S13 are shown in **Fig. S8**. The interionic RDFs are not considered.

## 2. Neutral atom (NA) model, screened point charge (SPC) model, and unscreened point charge (UPC) model

The three models of electrolyte solutions are simulated by applying different form factors of ions  $f_{ion}(q)$  in the IAM simulation. In the NA model, the ionic form factor simply equals to the atomic form factor of corresponding atoms.

$$f_{ion}(q) = f_{atom}(q). \quad (\text{Eq. S15})$$

For SPC and UPC models, the total ESP around the ion in real space can be written as:

$$\phi_{ion}(r) = \phi_{atom}(r) + \phi_{lr}(r). \quad (\text{Eq. S16})$$

Here, the  $\phi_{atom}(r)$  is the atomic ESP of the corresponding atom, and  $\phi_{lr}(r)$  is the extending long-ranged potential. In the SPC model, the long-ranged potential is partially screened and takes the form of a screened Debye–Hückel (DH) potential:

$$\phi_{lr,DH}(r, \lambda_D) = \pm \frac{\exp\left(-\frac{r}{\lambda_D}\right)}{r}. \quad (\text{Eq. S17})$$

Here,  $\lambda_D$  is the Debye screening length. The DH theory predicts the concentration dependence of  $\lambda_D$  at room temperature as  $\lambda_D(c) = \frac{3.07 \text{ \AA}}{\sqrt{\frac{c}{M}}}$ . This relation is used for

simulating the DH model curve in **Fig. 3** and **Fig. S8**. In the UPC model, the long-ranged ESP is unscreened and  $\phi_{lr}(r)$  takes a simple form of point charge as:

$$\phi_{lr,pc}(r) = \pm \frac{1}{r}. \quad (\text{Eq. S18})$$

The long-ranged potentials are smoothed to a finite value at  $r < 0.35 \text{ \AA}$  to avoid divergence at  $r = 0$ . The ionic form factor  $f_{ion}(q)$  is the Fourier transformation of the total ESP:

$$f_{ion}(q) = f_{atom}(q) + \int_0^{R_{max}} r^2 dr \frac{\sin(qr)}{qr} \phi_{lr}(r) e^{-\alpha r^2}. \quad (\text{Eq. S19})$$

Here,  $R_{max}$  is the cut off distance of  $\phi_{lr}(r)$ , and  $\alpha$  is the damping factor. The optimized parameter set should satisfy that  $R_{max} \gg \lambda_D$  and  $\alpha = \frac{10}{R_{max}^2}$ , so that the DH potential with screening length  $\lambda_D$  will not be cut off by the damping factor. In the simulation, the parameters are set as  $R_{max} = 5290 \text{ \AA}$  and  $\alpha = 3.57 \times 10^{-7} \text{ \AA}^{-2}$ . In order to compare directly with the experimental results, the simulated  $PDUC_{sim}(q)$  for slope fitting is convolved with a gaussian function with  $\text{FWHM} = 0.35 \text{ \AA}^{-1}$ , corresponding to a FWHM of 20 pixels on the EMCCD, to get the same  $q$  resolution as  $PDUC_{exp}(q)$ .

## 3. Ab-initio Molecular Dynamics Simulation

The RDFs are needed as the input for PDUC simulations. We setup a system to simulate the 0.1 mol/L ion concentration solvated by water molecules, which consists of an ion and ~500 water molecules with the periodic boundary condition (PBC) box size of  $25 \text{ \AA} \times 25 \text{ \AA} \times 25 \text{ \AA}$ . The Amoeba 2018 (33) polarizable force field was chosen to probably describe the influence of an ion in water with the ability to describe electronic polarization, with the induced dipole convergence threshold of 0.0001. The system was first minimized,

and followed by a 4 ns constant volume and temperature (NVT) simulation employing the reference system propagator algorithm (RESPA) (51) integrator and a time step of 2 fs. The temperature was maintained at 300 K using the velocity rescale (52) thermostat and a coupling time of 0.1 ps. The real-space Coulomb and van der Waals interactions were cut off at a distance of 12 angstroms. The particle mesh Ewald (53) method was cut off at 7 angstroms and the RETTLE (54) algorithm was used to constrain the water geometry. All of the classical MD equilibration and the RDF extraction were performed using the Tinker (55) software package.

All RDF results from simulation are plotted in **Fig. S8**. Note that the cations and anions are simulated separately, therefore the contribution of interionic interaction, which is concentration dependent, is not included in the simulation.

#### 4. Fitting the PDUC slope and the Debye lengths $\lambda_D$

The experimental and simulated PDUC slope value at  $0.4 \text{ \AA}^{-1}$  is obtained by the linear least-square fitting of PDUC points between  $0.35$  and  $0.45 \text{ \AA}^{-1}$ . The results are plotted in **Fig. S9**. By fitting the simulated PDUC with different  $\lambda_D$  values, a one-to-one relationship is established between  $\lambda_D$  and the slope value at  $0.4 \text{ \AA}^{-1}$ . From this relationship and the experimental PDUC slope, the  $\lambda_D$  values can be read out. The maximum PDUC slope corresponds to  $\lambda_D = 2 \text{ \AA}$ , which gives the lowest limit of the retrievable  $\lambda_D$  value using this method.

#### 5. Nonlocal dielectric function (NLDF) retrieval

The static NLDF  $\varepsilon(q)$  is defined by

$$\phi_{ind}(q) + \phi_{ext}(q) = \frac{1}{\varepsilon(q)} \phi_{ext}(q). \quad (\text{Eq. S20})$$

Here,  $\phi_{ext}(q)$  is the Fourier transformation of the external ESP, and  $\phi_{ind}(q)$  is the induced ESP. In electrolyte solutions,  $\phi_{ext}(q)$  can be interpreted as the long-ranged ESP exerted by an ion, and  $\phi_{ind}(q) + \phi_{ext}(q)$  the screened ESP of this ion. Taking the form of DH potential in the SPC model,  $\phi_{ext}(q)$  and  $\phi_{ind}(q)$  can be calculated as:

$$\phi_{ext}(q) = \mathcal{F} \left[ \pm \frac{1}{r} \right] = \pm \frac{4\pi}{q^2}, \quad (\text{Eq. S21})$$

$$\phi_{ind}(q, \lambda_D) + \phi_{ext}(q) = \mathcal{F} \left[ \pm \frac{\exp(-\frac{r}{\lambda_D})}{r} \right] = \pm \frac{4\pi}{\lambda_D^2 + q^2}. \quad (\text{Eq. S22})$$

Substitute into Eq. S20, and the NLDF is obtained as:

$$\varepsilon_{DH}(q, \lambda_D) = 1 + \frac{1}{\lambda_D^2 q^2}. \quad (\text{Eq. S23})$$

This expression of NLDF is consistent with the Thomas-Fermi (TF) model that  $\varepsilon_{TF}(q, k_F) = 1 + \frac{k_F^2}{q^2}$  with  $k_F = \frac{1}{\lambda_D}$ . From the concept in Fig. 3C, the NLDF retrieved from PDUC curves can be described as

$$\varepsilon_{ret}(q, \lambda_D) = \sqrt{\frac{PDUC_{UPC}(q) - PDUC_{NA}(q)}{PDUC_{SPC}(q, \lambda_D) - PDUC_{NA}(q)}}. \quad (\text{Eq. S24})$$

Eq. S23 and Eq. S24 give equivalent results of NLDF under perfect  $q$  resolution. This is verified by following steps: 1) Simulating a mock electron scattering pattern of aqueous KCl solution under the NA model, UPC model, and SPC model using three different  $\lambda_D$  values (3.07 Å, 9.71 Å, 30.7 Å). 2) Extract the  $PDUC_{UPC}(q)$ ,  $PDUC_{NA}(q)$ , and  $PDUC_{SPC}(q, \lambda_D)$  from the simulated scattering patterns. 3) Retrieve the  $\varepsilon_{ret}(q, \lambda_D)$  using Eq. S24. The retrieved  $\varepsilon_{ret}(q, \lambda_D)$  reproduces the input  $\varepsilon_{TF}(q, k_F)$  very well, as shown in **Fig. S10A**.

An impact of  $q$  resolution on the PDUC signal is shown in **Fig. S14C**. Eq. S24 requires the PDUC signal with a perfect  $q$  resolution, which is not achieved experimentally. To eliminate the impact of the  $q$  resolution, experimental PDUC curves are first mapped into simulated  $PDUC_{SPC}(q, \lambda_D)$  with perfect  $q$  resolution, through the  $\lambda_D$  fitting at 0.4 Å<sup>-1</sup>. The NLDF value is then computed using Eq. S24.

The obtained NLDF value will have a  $q$  dependent up-limit, which can be roughly estimated by  $\sqrt{\frac{PDUC_{UPC}(q) - PDUC_{NA}(q)}{PDUC_{NA}(q)}}$ . This is because that a measurable NLDF value requires that the difference between  $PDUC_{SPC}(q)$  and  $PDUC_{NA}(q)$  should be distinguishable from experimental background. A larger measurable value of NLDF can be obtained at the  $q$  range where  $PDUC_{UPC}(q) \gg PDUC_{NA}(q)$ , so that a larger difference between  $PDUC_{SPC}(q)$  and  $PDUC_{NA}(q)$  exists. This also accounts for the low-limit of  $\lambda_D$ , where the difference between  $PDUC_{SPC}(q)$  and  $PDUC_{NA}(q)$  cannot be distinguished. The estimated  $q$  dependent up-limit of NLDF is shown in **Fig. S10B**, with  $\varepsilon_{max} \sim 4$  at 0.4 Å<sup>-1</sup>. This is the theoretical upper limit that only considers the background from leftover atomic form factors. Additional experimental backgrounds can further reduce this upper limit. In our work, the upper limit  $\varepsilon_{max} = 2.6$  is obtained from the lowest retrievable  $\lambda_{D,min} = 2$  Å.

## Supplementary Text

### Quantitative understanding of atomic vs ionic electron scattering form factor

The electron form factor of an atom is described by the Mott-Bethe formula (29, 30):

$$f_e(q) = \frac{\gamma m}{2\pi\hbar^2} \frac{Z - f_X(q)}{q^2} \quad (\text{Eq. S25})$$

Here,  $q$  is the momentum transfer,  $\gamma m$  is the relativistic mass of the incident electrons,  $\hbar$  is the reduced Planck constant,  $Z$  is the nuclei charge of the target atom, and  $f_X(q)$  is the Fourier transform of the electron density, also known as the X-ray atomic scattering form factor.  $Z - f_X(q)$  represents the screening of the ESP, i.e. the nuclear charge  $Z$  is screened by the electron cloud  $f_X$ . The theoretical atomic form factors for neutral K atom and K<sup>+</sup> cation are shown in the main text, and a significant difference between the two is observed at small  $q$ . This can be understood by the difference in the long-range ESP distribution. For atoms,  $f_X(q) \rightarrow Z$  as  $q \rightarrow 0$ , and  $\frac{Z - f_X(q)}{q^2}$  converges to a finite number,

indicating that ESP distribution is short-ranged when the nuclear ESP is perfectly screened by the electron cloud. For monovalent cation,  $f_X(q) \rightarrow Z \pm 1$  as  $q \rightarrow 0$ , leading to a diverging  $\frac{Z-f_X(q)}{q^2}$  as  $q \rightarrow 0$ , indicating that the ESP distribution is long-ranged when the nuclear ESP is underscreened.

### Measurement of structure vs interaction using electron scattering

The elastic electron scattering amplitude can be described equivalently by two formula (56):

$$I_{ela}(\vec{q}) = \left( \frac{\gamma m}{2\pi\hbar^2} \right)^2 |\mathcal{F}[\phi(\vec{r})]|^2, \quad (\text{Eq. S26})$$

$$I_{ela}(\vec{q}) = \left( \frac{\gamma m}{2\pi\hbar^2} \right)^2 \frac{1}{q^4} |\mathcal{F}[\rho(\vec{r})]|^2, \quad (\text{Eq. S27})$$

where  $\phi(\vec{r})$  is the ESP of the system,  $\rho(\vec{r})$  is the charge density (including both electrons and nuclei) of the system, and  $\mathcal{F}$  represents a Fourier transform.  $\phi(\vec{r})$  and  $\rho(\vec{r})$  are connected by the following equation

$$\phi(\vec{r}) = \int d^3\vec{r}' \frac{\rho(\vec{r}')}{|\vec{r} - \vec{r}'|}. \quad (\text{Eq. S28})$$

Eq. S27 was first derived by Bethe, by applying a Green-function type integral known as the Bethe integral (30). The vast majority of electron scattering works so far have been based on Eq. S27, where the  $\rho(\vec{r})$  is the primary unknown, which is directly connected to structure. This work is based on Eq. S26, where  $\phi(\vec{r})$  is the primary unknown. Eq. S26-S27 show that electron scattering can be used to measure both the structure  $\rho(\vec{r})$  and the interaction  $\phi(\vec{r})$ .

### The impact of inelastic scattering

The total scattering intensity measured in experiment is composed of elastic and inelastic scattering intensity that  $I_{tot}(q) = I_{ela}(q) + I_{ine}(q)$ , and the experimental PDUC can be described as

$$PDUC_{exp}(q) = \frac{(I_{s,ela}(q) - I_{w,ela}(q)) + (I_{s,ine}(q) - I_{w,ine}(q))}{I_{w,ela}(q) + I_{w,ine}(q)}, \quad (\text{Eq. S29})$$

where subscript *s* and *w* represent the solution and water, respectively.

The inelastic scattering appears on both the numerator and the denominator. At small  $q$ , the inelastic scattering dominates over the elastic scattering for neutral water molecules, but is negligible in comparison to the elastic scattering signal from a point charge, as shown in **Fig. S11A**. Therefore, the inelastic scattering term can be ignored in the numerator for solution with long-ranged ESP distribution but must be considered in the denominator.

An accurate simulation of inelastic scattering in liquid requires full quantum mechanical level treatment of electron-electron correlations, which is beyond the capability by existing ab-initio quantum chemistry methods. Here we use the tabulated IAM inelastic cross-section for a rough estimation (57). According to a high-level quantum simulation of inelastic electron scattering for a single water molecule in the gas phase, IAM overestimates the inelastic scattering signal by 15-20% (**Fig. S11B**). For liquid water, we expect this overestimation to be even higher. For the inelastic scattering term on the denominator, this could reduce the PDUC and the slope value by at least 20%. To balance

this overestimation, we ignore the two hydrogen atoms and only use the IAM inelastic scattering cross-section of the oxygen atom to represent the water molecule. In addition, **Fig. S11C-D** simulates the impact of inelastic scattering in the numerator, which shows that it gives a constant shift of the PDUC values, and makes no difference once the slopes of the PDUC curves are taken.

For the reasons above, the simulated PDUC curves in the main text (Fig. 2A-B, Fig. 3C) are calculated using the equation below

$$PDUC_{sim}(q) = \frac{I_{s,ela}^{IAM}(q) - I_{w,ela}^{IAM}(q)}{I_{w,ela}^{IAM}(q) + S_0(q)}, \quad (\text{Eq. S30})$$

where  $S_0(q)$  is the inelastic form factor of O atom.

#### Charge-pair distribution function (CPDF)

CPDF was proposed as a method to retrieve liquid structure from LES data (27). The hydration structure of ions can be retrieved by taking the difference of interatomic CPDF of electrolyte solution and water as

$$\Delta CPDF_{inter}(r) = r^2 \int_0^{q_{max}} q^2 dq \frac{\sin(qr)}{qr} q^4 (I_{s,mol}(q) - I_{w,mol}(q)) e^{-\alpha q^2}. \quad (\text{Eq. S31})$$

Here,  $I_{s,mol}(q)$  and  $I_{w,mol}(q)$  are the molecular scattering intensities of the solution and water. In the experiment,  $I_{mol}(q)$  for the solution and water is obtained by removing a background function  $I_{bkg}(q)$  (containing the atomic and inelastic scattering term) as  $I_{exp,mol}(q) = I_{exp,tot}(q) - I_{bkg}(q)$ . The  $I_{bkg}(q)$  is fitted by a series of exponential functions of  $Ae^{-cq^b}$ , following the background extraction method proposed by Zewail (58). The  $\Delta CPDF$  can also be simulated using the IAM molecular scattering result as:

$$\Delta CPDF_{sim}(r) = r^2 \int_0^{q_{max}} q^2 dq \frac{\sin(qr)}{qr} q^4 I_{ion,mol}(q) e^{-\alpha q^2}. \quad (\text{Eq. S32})$$

**Fig. S12** shows the results of the three samples in concentrations of 250, 500 and 1000 mM, with comparison to RDF hydration shell positions and corresponding  $\Delta CPDF$  simulations. In the concentration above 500 mM, first hydration shell positions of all three samples match very well with the RDF result. At lower concentrations, the noise in the large  $q$  range significantly increases and disturbs the real space structure information.

#### Electron penetration depth and liquid sheet thickness

The liquid sheet thickness  $d$  can be characterized by the electron beam transmittance  $T$  based on Lambert-Beer's law as:

$$-\log(T) = \sigma \rho_0 d \quad (\text{Eq. S33})$$

Here,  $\sigma$  is the cross section of water molecule under IAM approximation, and  $\rho_0$  is the number density of water. Define the penetration depth  $\Lambda$  as:

$$\Lambda = \frac{1}{\sigma \rho_0} \quad (\text{Eq. S34})$$

For 1.7 MeV electron beam, the elastic penetration depth  $\Lambda_{ela} = 960$  nm. The average transmittance in experiment is about 30%, corresponding to an estimated liquid sheet thickness of 500 nm (**Fig. S13A**).

#### Multiple-scattering effect

The liquid sheet of water and electrolyte solutions may have different thicknesses. Under single-scattering regime, it can be normalized by total counts. Under multiple-scattering regime, however, it might change the ratio between different multiple-scattering levels and cannot be simply calibrated by total count normalization. In order to assess the possible contribution of multi-scattering in our final signal, we collect LES signal from 4 different thicknesses of neat water: 286 nm, 337 nm, 387 nm, and 483 nm, as estimated by Eq. S33 respectively. Define the percentage difference (PD) with respect to the scattering intensity on thickest position as:

$$PD(d) = \frac{I(d) - I(d = 483 \text{ nm})}{I(d = 483 \text{ nm})} \quad (\text{Eq. S35})$$

The PD curves of  $d = 286, 337$ , and  $387 \text{ nm}$  are shown in **Fig. S13B-E**. At large  $q$  range, the difference of thickness contributes to a slow-varying structureless background. At small  $q$ , especially  $q < 0.3 \text{ \AA}^{-1}$ , the PD curves have a significant monotonous rise, because for thinner liquid sheet, the electron beam will have a larger transmittance. In comparison, the PDUC signal from the electrolyte solution appear as a completely different shape: it rises sharply at  $0.4\text{--}0.5 \text{ \AA}^{-1}$ , reaches the maximum at  $0.3 \text{ \AA}^{-1}$ , and decreases to negative value at  $q < 0.3 \text{ \AA}^{-1}$  (red curve in **Fig. 13D**). Therefore, we conclude that the multiple-scattering effect is unlikely to have any appreciable contributions to the observed PDUC signals for electrolyte solutions.

#### Electron beam size and $q$ resolution

The experimental electron beam is oval shaped, with FWHM of long axis 16~20 pixels ( $0.28\text{--}0.35 \text{ \AA}^{-1}$ ) and short axis 12~14 pixels ( $0.21\text{--}0.25 \text{ \AA}^{-1}$ ). The azimuthal averaged intensity of electron beam and the ratio of electron beam intensity over water scattering intensity,  $\frac{I_{mb}(q)}{I_w(q)}$ , are shown in **Fig. S14A-B**. The 1-D electron beam intensity decays to less than 20% of the scattering intensity of water at  $0.3 \text{ \AA}^{-1}$ , and dropped to less than 5% at  $q > 0.4 \text{ \AA}^{-1}$ .

The  $q$  resolution, determined by electron beam size, will significantly affect the PDUC result at small angles. Define the  $q$  resolution as the maximum of the FWHM of electron beam ( $0.35 \text{ \AA}^{-1}$  for current experimental results). Simulated PDUC curves of KCl solution with different resolutions are shown in **Fig. S14C**. Different  $q$  resolutions are simulated by convolving the full resolution PDUC with a gaussian function with different FWHMs. By improving the  $q$  resolution, PDUC value at smaller  $q$  range can be measured with higher precision. This also enables a larger measurable upper limit of NLDF and makes it possible to measure the ESP distribution at different  $q$  points, i.e. on different length scales in real space.

#### Liquid sample temperature estimation

The liquid sample temperature can be estimated using the ratio of the second OO peak ( $g_2$ ) to the first OO peak ( $g_1$ ) in CPDF of water (28). Using the same method, it is estimated that the temperature of water sample (at the position of electron beam) is 280 K (**Fig. S15**).

#### Impact of in-vacuum evaporation on concentration

The liquid sheet will evaporate under vacuum, which might change the concentration at the interaction point. Here we give a rough estimation of this effect.

At the room temperature of 293 K, the maximum evaporation flux of liquid water surface in vacuum is  $1.421 \times 10^{-3} \text{ mol cm}^{-2} \text{ s}^{-1}$  (estimated from the evaporation rate equation) (59), and the corresponding thickness loss rate is  $256 \mu\text{m/s}$ . Considering the liquid sheet has two surfaces, the thickness loss rate should double. The size of the chip outlet is  $20 \mu\text{m}$  thick and  $100 \mu\text{m}$  wide. Under the liquid flux of  $4 \text{ ml/min}$ , the liquid velocity is  $33 \text{ m/s}$ . The liquid sheet will keep in contact with vacuum for about  $3 \text{ mm}$  until reaching the position of electron beam, which gives an evaporation time of  $9 \times 10^{-5} \text{ s}$ . The thickness loss during this time is  $0.046 \mu\text{m}$ . Compared with the outlet thickness  $20 \mu\text{m}$ , only  $\sim 0.23\%$  of water evaporates at the interaction point, which makes negligible impact on the sample concentration.

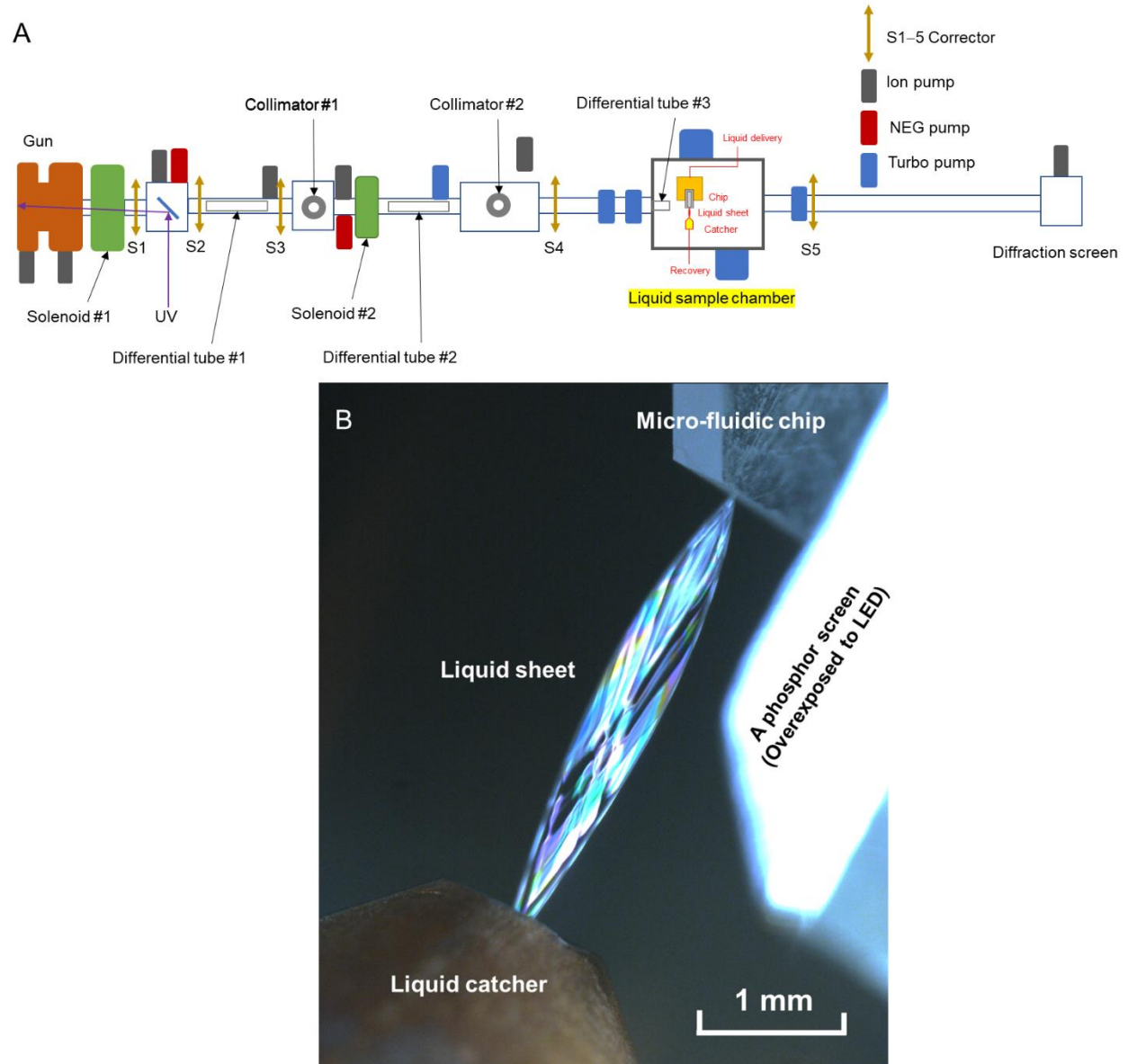


**Fig. S1.**

(A) Diagrams of the LES beamline in Tsinghua University. (B) A photo of liquid sheet in the chamber (with sample chamber pressure of  $3e-3$  Torr).

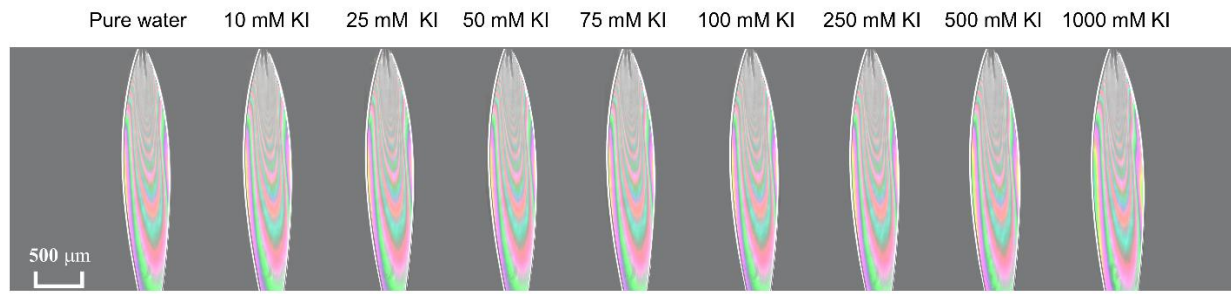


**Fig. S2.**

The photos of liquid sheet of aqueous KI at atmosphere condition. The liquid flow velocity is 4 mL/min and the interferometric fringe is produced from a white LED lighting.

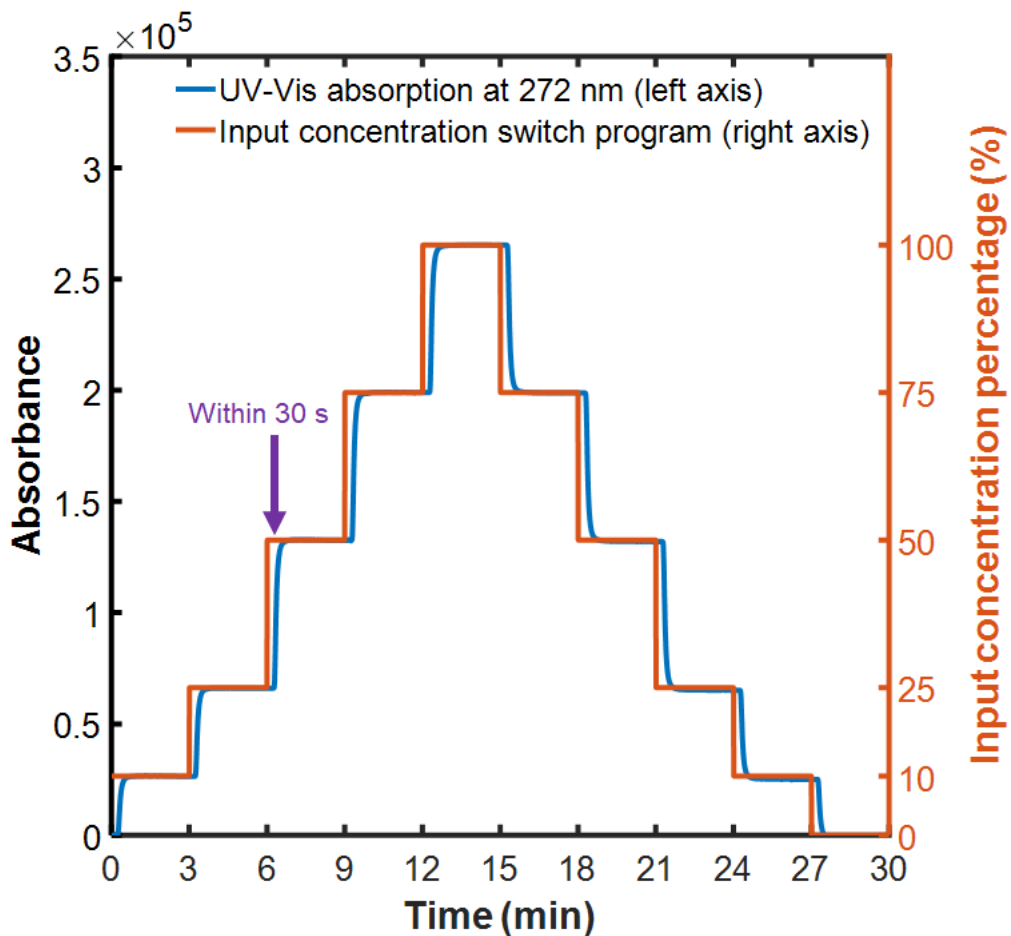


**Fig. S3.**

Measurement of the liquid sample switching time by real-time UV-Vis spectroscopy measurement of standard caffeine solution on the liquid sheet. Concentration of caffeine solution was changed by switching the low-pressure gradient valve at 0, 3, 6, 9, 12, 15, 18, 21, 24, 27, and 30-minute mark, with a setting value of 10, 25, 50, 75, 100, 75, 50, 25, 10, and 0 percent, respectively. The desired concentration is achieved within 30 seconds of each switch.

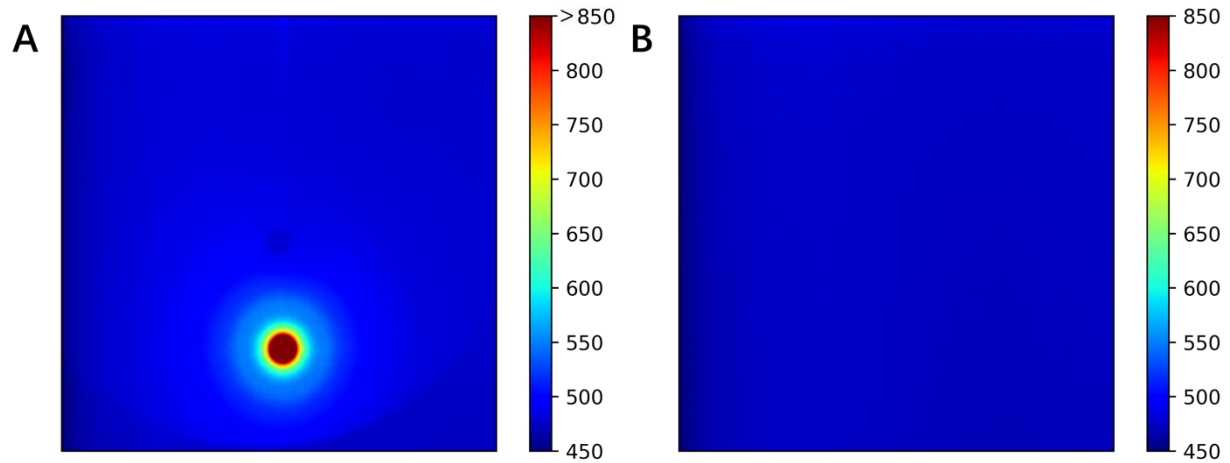


**Fig. S4.**

(A) The median pattern of 250 raw scattering patterns. (B) The median pattern of 100 EMCCD background patterns, taken without the electron beam.

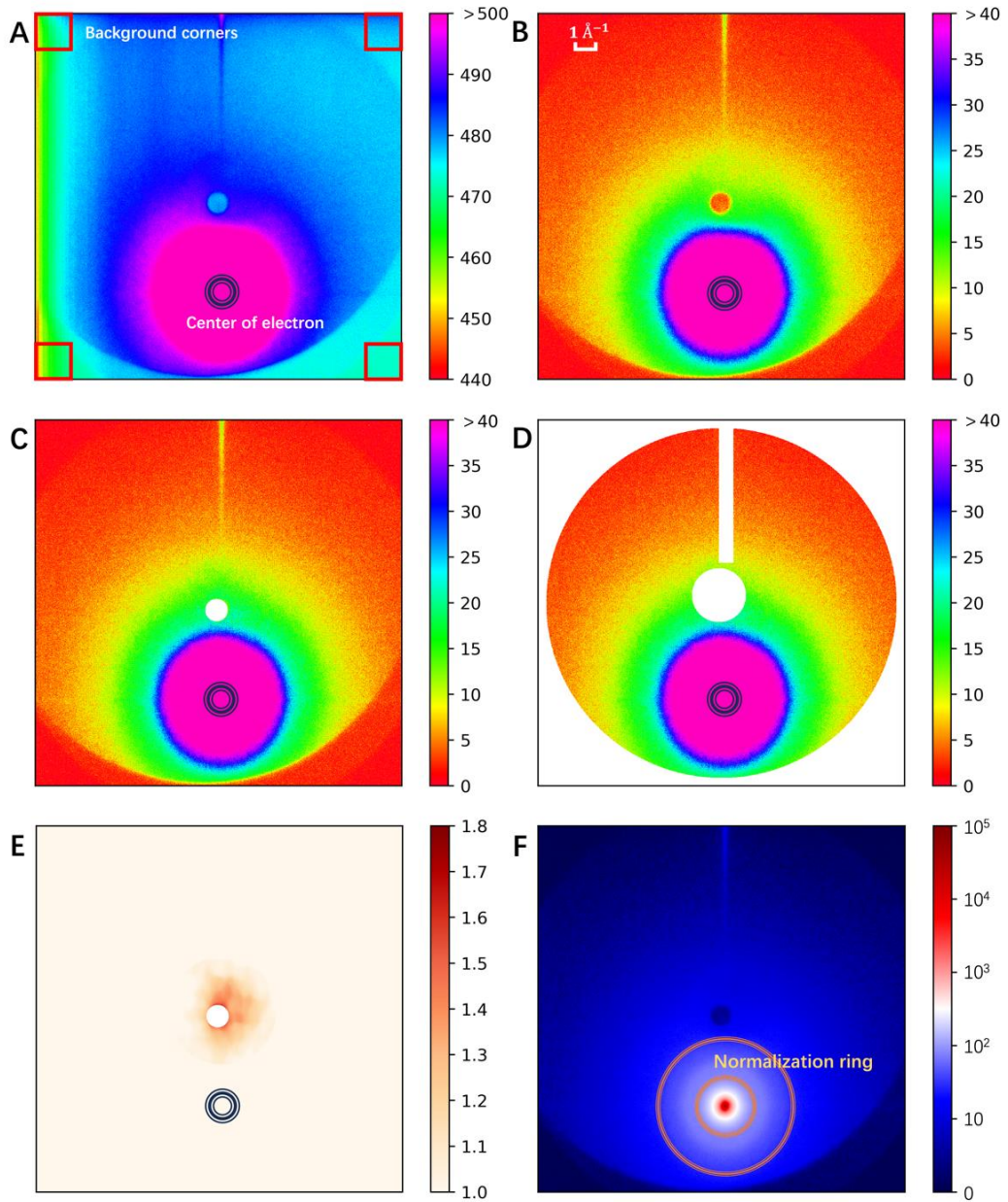


**Fig. S5.**

Diagrams of the pattern treatment including background removal, gain-map calibration, mask treatment, and total count normalization, with 250 patterns of water as an example. The concentric circles in (A-E) mark the position of electron beam. (A) The median pattern of 250 raw patterns. The 4 red squares mark out the background corners. (B) The median pattern of the 250 background-removed patterns. (C) The median pattern after gain-map calibration (by multiplying pattern (B) with gain-map (E)). (D) Mask treatment of pattern (C). (E) The gain-map pattern. (F) The total count normalization ring, marked out by the two orange concentric circles with the radius of 1.5 and  $3.3\text{\AA}^{-1}$ , respectively.

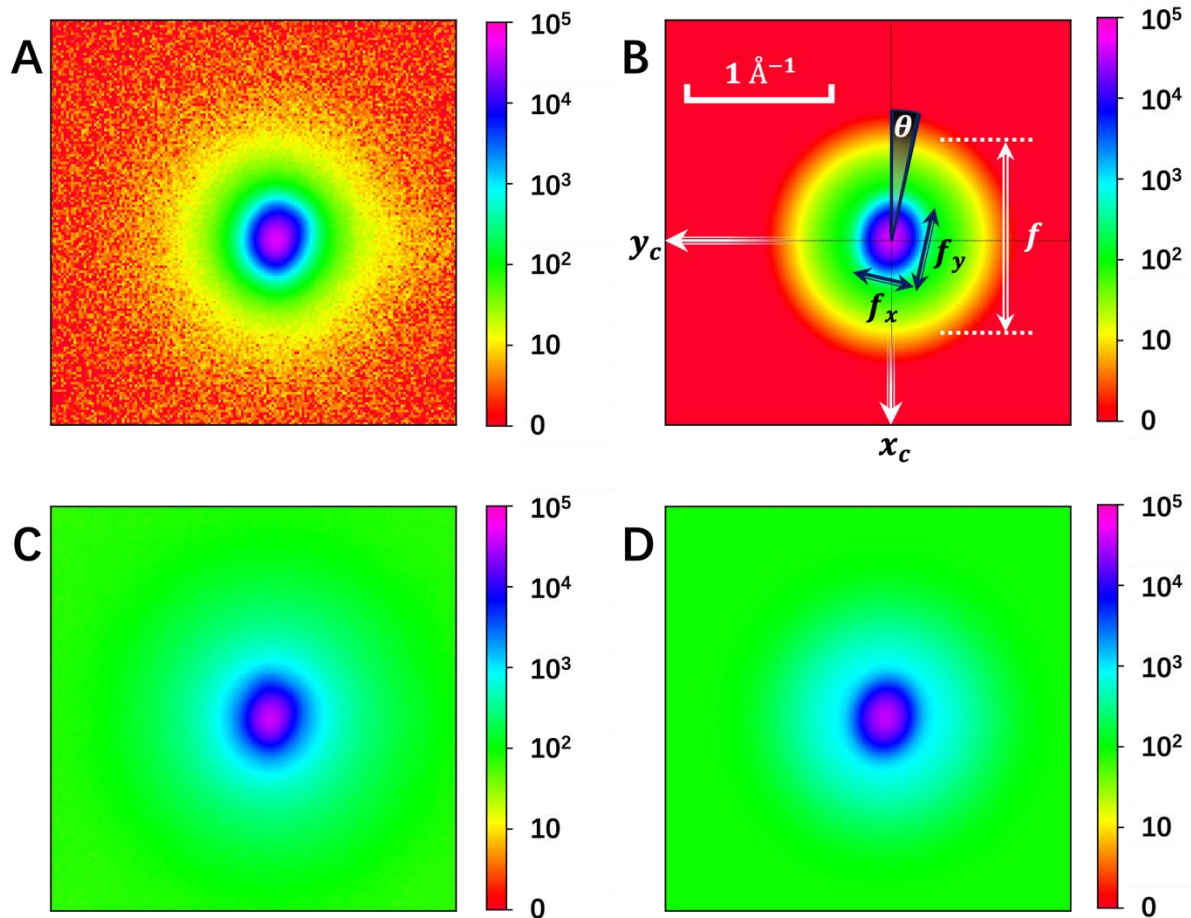


**Fig. S6.**

(A) A zoom-in pattern of electron beam (without sample), obtained by the median of 100 background-removed patterns. (B) The fitted result of pattern (A), with 6 fitting parameters ( $x_c, y_c, \theta, f_x, f_y, f$ ) depicted. (C) A zoom-in scattering pattern of water sample under the same experimental condition as (A), as the median of 250 background-removed. (D) The fitted result of pattern (C).

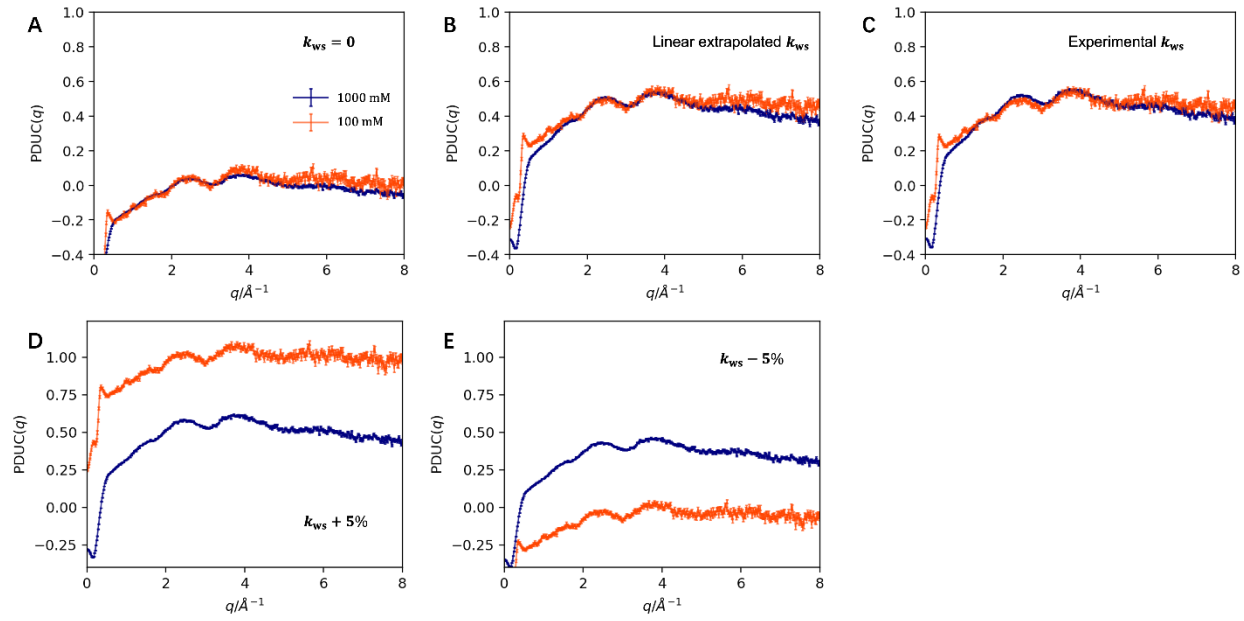


**Fig. S7.**

Experimental PDUC curves of 1000 mM and 100 mM KI solution, after total count normalization, with different water-salt balance coefficients. (A) PDUC curves without water-salt balance coefficient. The two curves match with each other due to total count normalization. (B) PDUC curves with water-salt balance coefficients linear extrapolated from 500 mM measurement. The two concentrations match with each other at medium to large  $q$  range. (C) PDUC curves with water-salt balance coefficients measured from density experiment. (D-E) PDUC curves with the water-salt balance constant reduced or amplified by 5%. A large deviation is observed between the two concentrations.

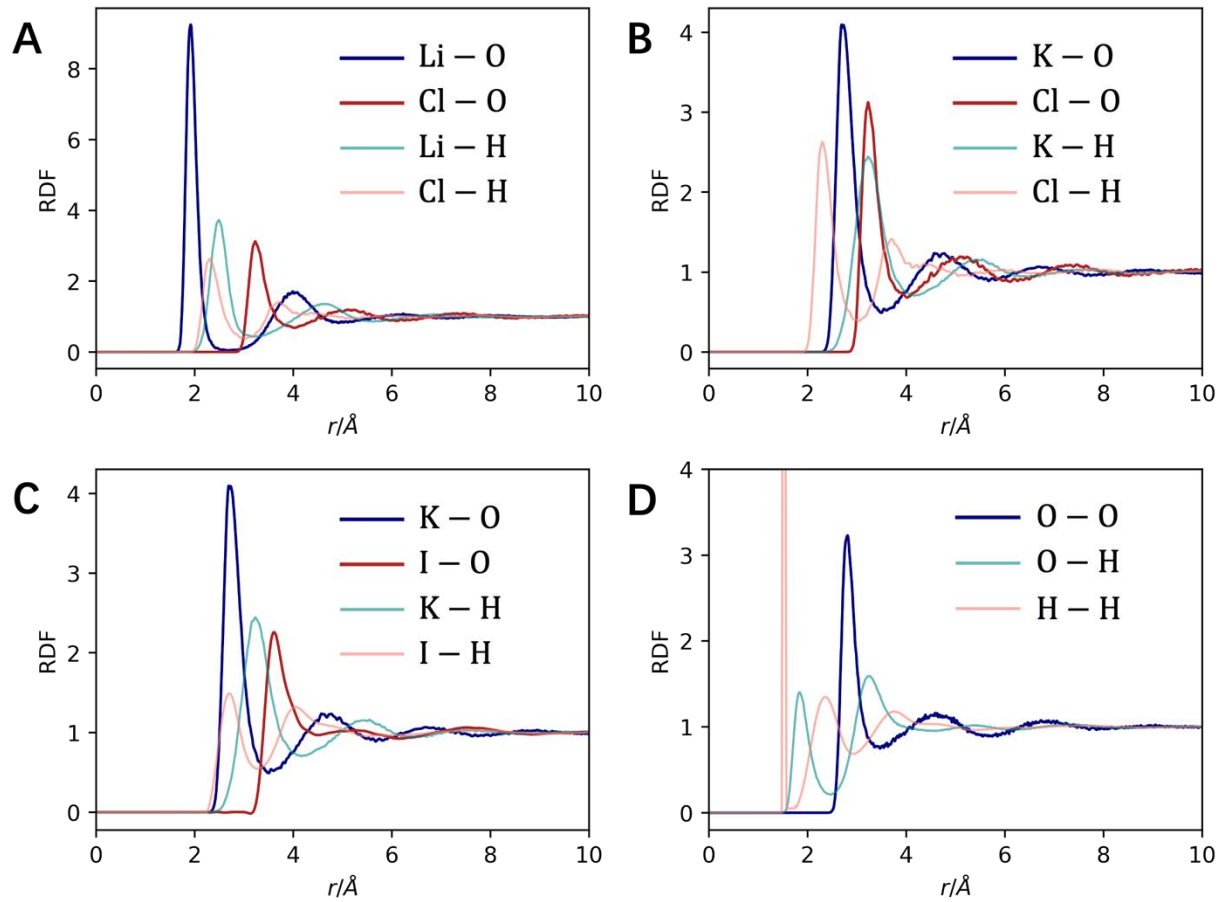


**Fig. S8.**

(A-D) Simulated RDF results for LiCl (A), KCl (B), KI (C) and water (D), respectively.

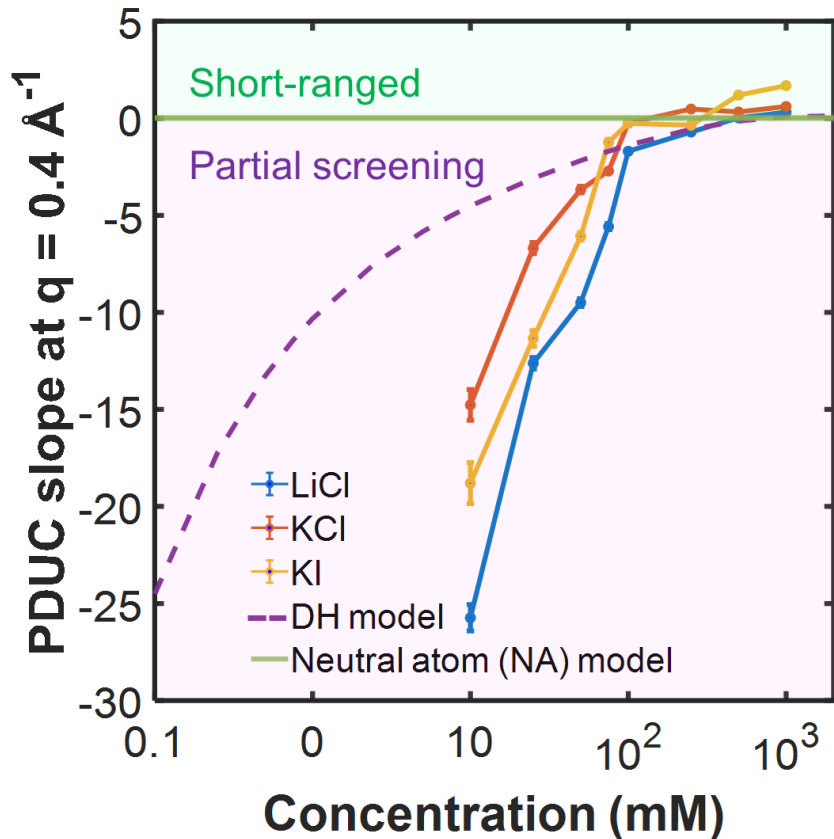


**Fig. S9.**

Fitted PDUC slope at  $q = 0.4 \text{ \AA}^{-1}$  for different samples at different concentrations, together with the Debye-Hückel (DH) model and the neutral atom (NA) model.

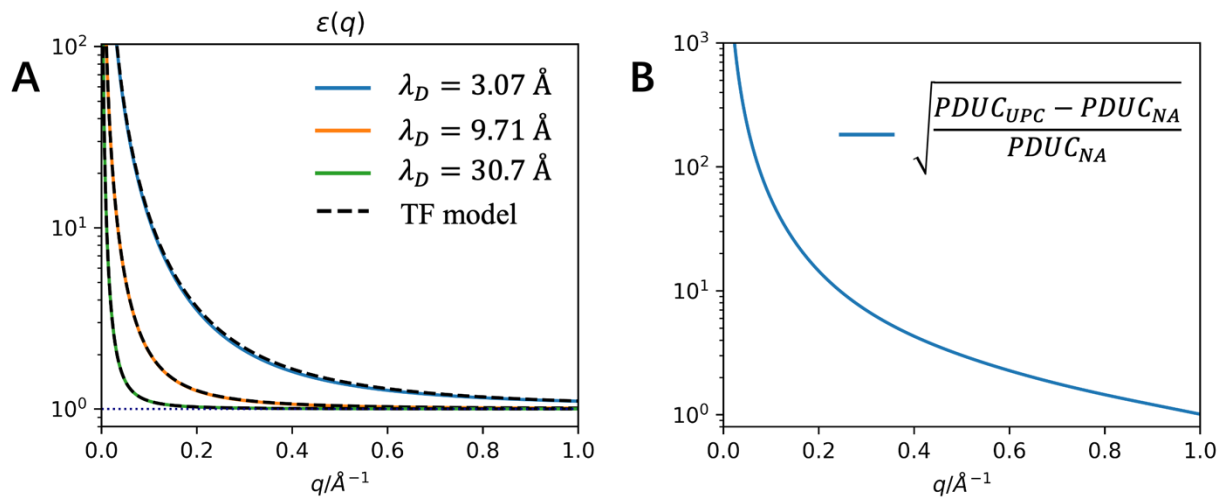


**Fig. S10.**

(A)  $\varepsilon_{ret}(q, \lambda_D)$  curves retrieved from Eq. S24 for three different  $\lambda_D$  values, and the corresponding results from TF model simulated with Eq. S23. (B) The estimated measurable NLDF up-limit.

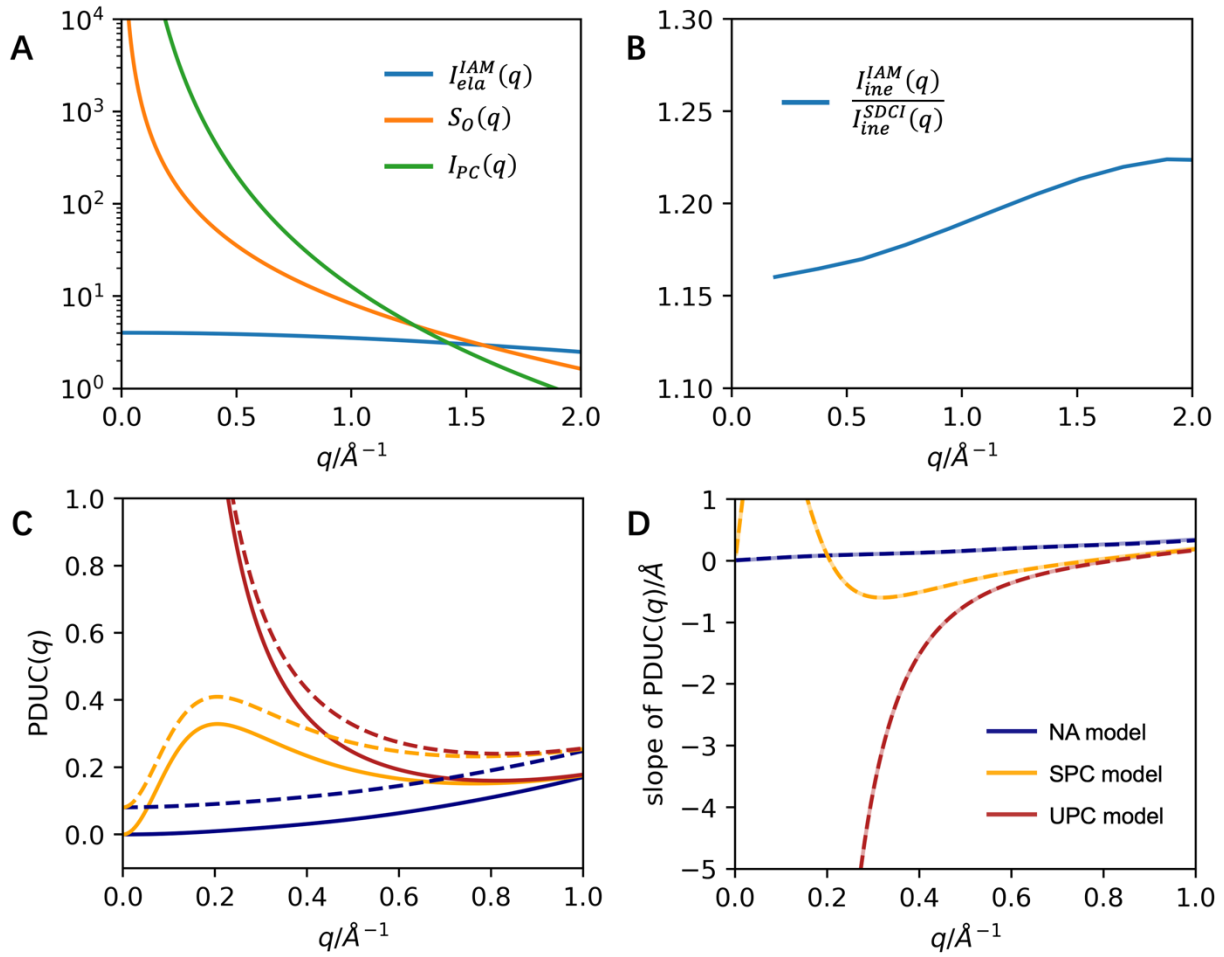


**Fig. S11.**

(A) the IAM elastic scattering intensity of neutral water molecule, the inelastic scattering form factor of O atom  $S_o(q)$ , and the elastic scattering intensity of a point charge, y axis is in atomic unit. (B) The ratio of IAM and single-double configuration-interaction (SDCI) inelastic scattering intensity. The SDCl inelastic scattering intensity is taken from literature (60). (C) The PDUC curves and (D) the slope of PDUC curves of simulated KI solution. The solid lines are simulated with  $I_{s,ine}(q) = I_{w,ine}(q) = S_o(q)$ , while the dashed lines taking into account the IAM inelastic scattering of I atom that  $I_{s,ine}(q) = S_o(q) + S_I(q)$ , where  $S_I(q)$  is the inelastic form factor of I atom. Three colors represent three screening models of the ion.

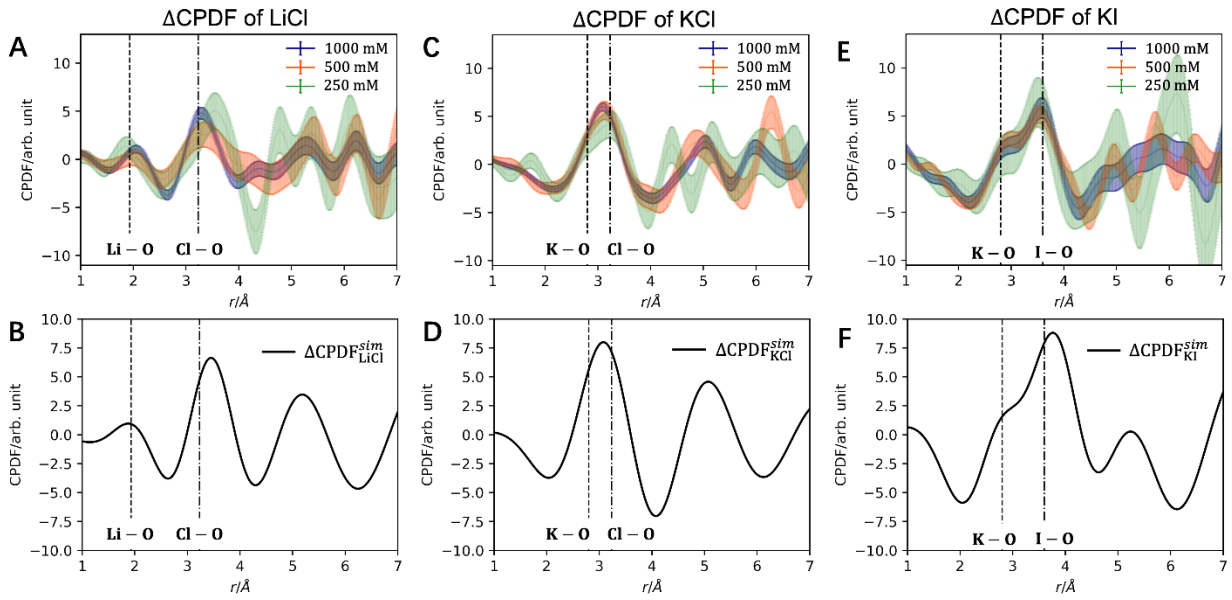


**Fig. S12.**

(A, C, E) Experimental  $\Delta\text{CPDF}$  curves of LiCl (A), KCl (C), and KI (E) at the concentration of 1000, 500 and 250 mM. Shades represent error bars, obtained from one S.E.M. of 300-600 independent measurements. The damping factor is set to  $\alpha = 0.06 \text{ \AA}^2$  in this calculation. The dashed line marks the first hydration shell position (from the simulated RDF) of the cation and the dash-dotted line marks that of the anion. (B, D, F) Simulated  $\Delta\text{CPDF}$  curves of KI (B), KCl (D) and LiCl (F) under IAM approximation with  $q_{\text{max}} = 12 \text{ \AA}^{-1}$  and  $\alpha = 0.15 \text{ \AA}^2$ .

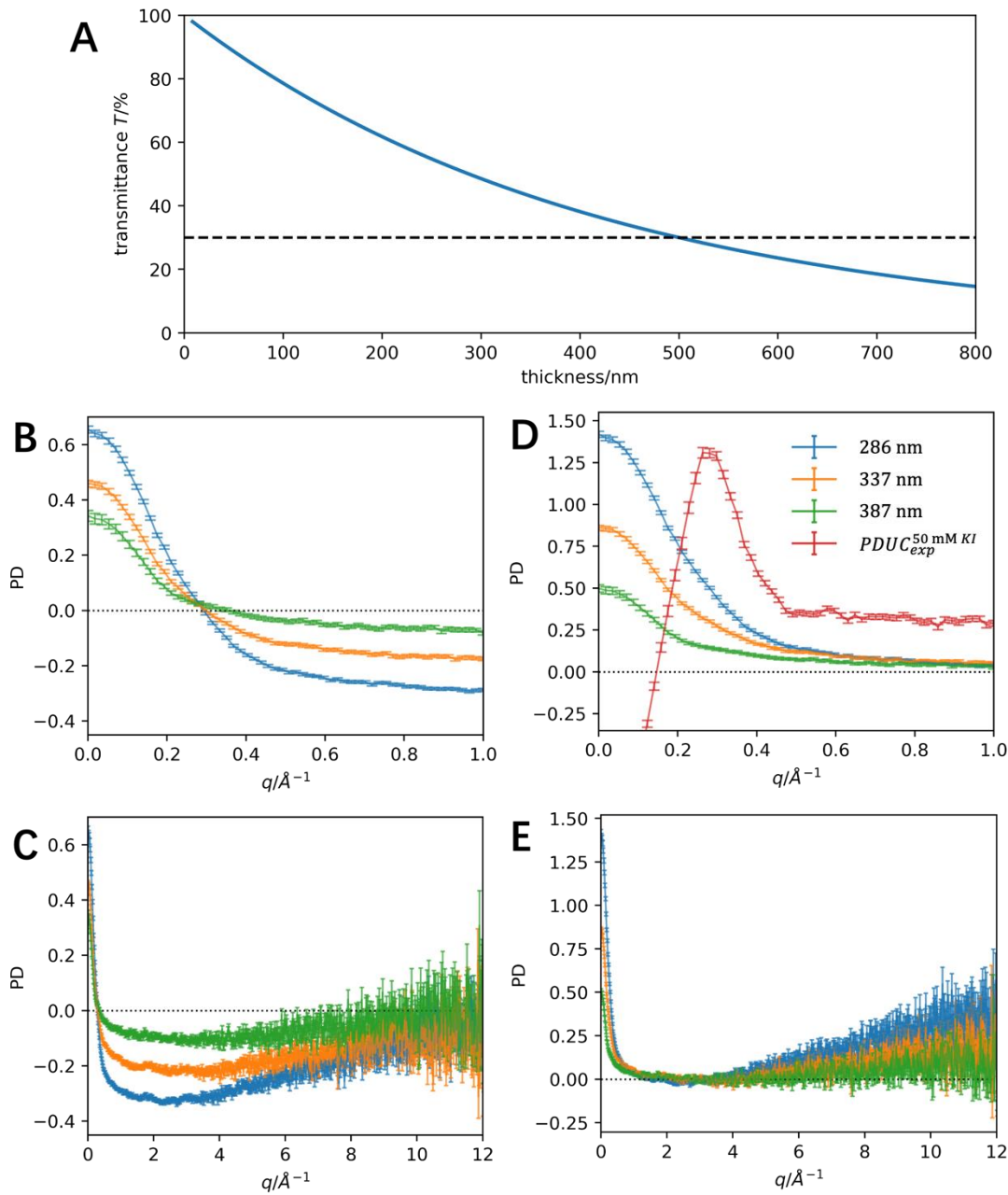


**Fig. S13.**

(A) The relation between electron beam transmittance and the liquid sheet thickness, calculated using Eq. S33. The dashed black line marks the experimental transmittance of 30%. (B-E) PD curves of water scattering intensity at thickness  $d = 286, 337$  and  $387$  nm with respect to thickness  $d = 483$  nm. PD curves in (B) and (C) are calculated from unnormalized scattering intensity, while (D) and (E) are calculated from total count normalized scattering intensity. The experimental PDUC curve of  $50 \text{ mM KI}$  solution is plotted in (D) for direct comparison.

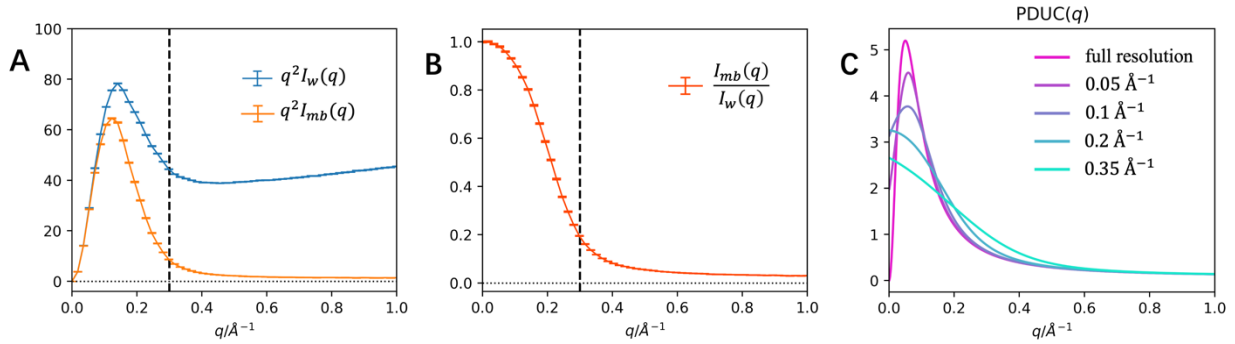


**Fig. S14.**

(A) The azimuthal averaged intensity of the electron main beam (denoted by  $I_{mb}(q)$ ) and water (denoted by  $I_w(q)$ ), both multiplied by  $q^2$ .  $I_w(q)$  is normalized to have the same intensity as  $I_{mb}(q)$  at the beam center. Error bars for  $I_{mb}(q)$  and  $I_w(q)$ , one S.E.M. of 100 and 250 independent measurements, respectively. (B) The ratio of electron beam intensity over water scattering intensity,  $\frac{I_{mb}(q)}{I_w(q)}$ . The dashed line in (A) and (B) marks the  $q = 0.3 \text{\AA}^{-1}$  line. (C) Simulated PDUC curves of KCl solution with different  $q$  resolutions.

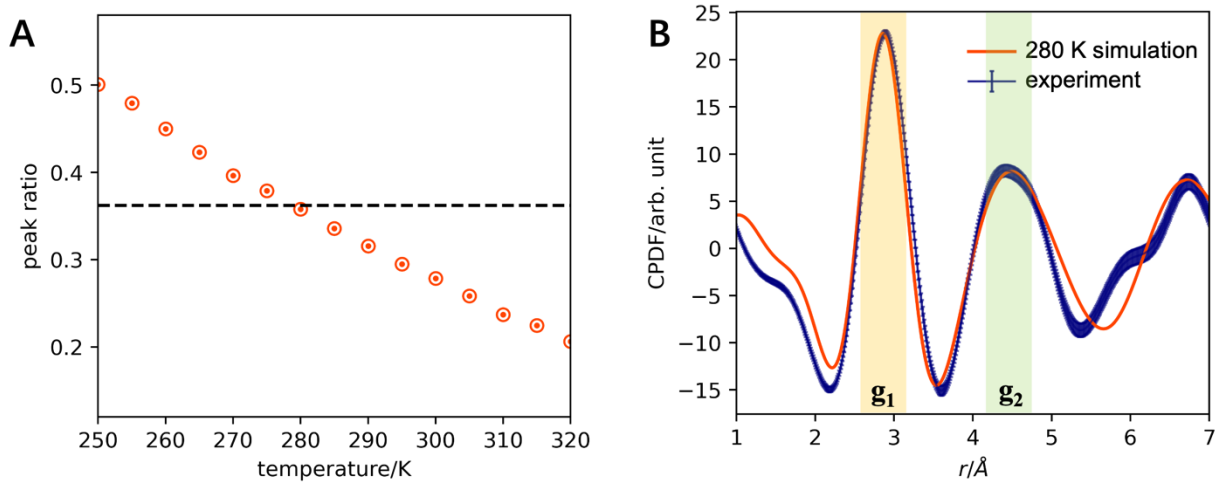


**Fig. S15.**

Temperature measurement. (A) The ratio of the second OO peak maximum ( $g_2$ ) to the first OO peak maximum ( $g_1$ ) in neat water CPDF. Red dots: peak ratio values of simulated CPDFs at different temperatures. Dashed black line: the experimental value. (B) The experimental CPDF of neat water and the simulated CPDF under 280 K.

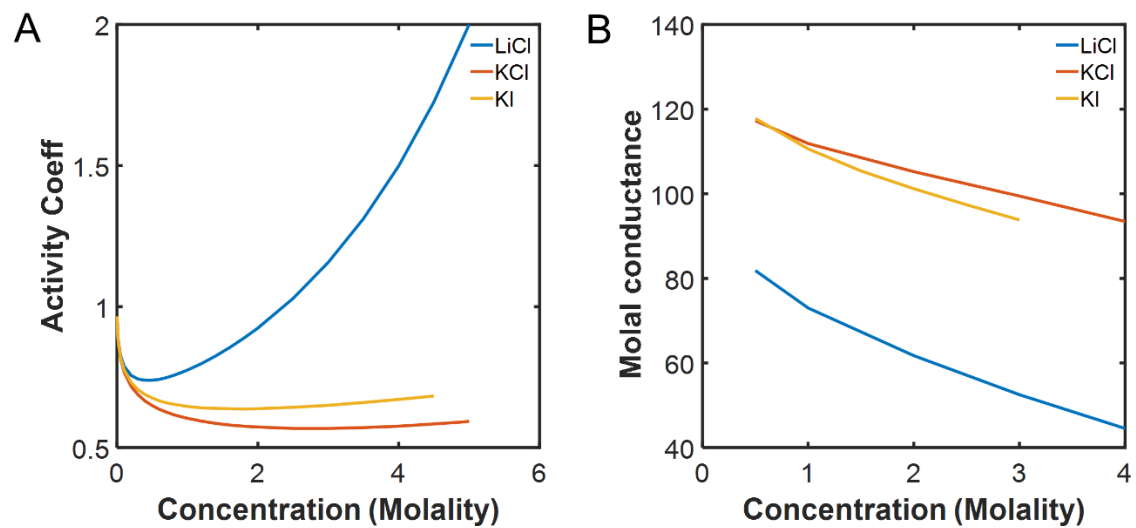


**Fig. S16.**

Activity coefficient (A) and molal conductance (B) as a function of concentration for LiCl, KCl, and KI, respectively. Data extracted from ref. (48) and (49).

Concentration (mM)	LiCl	KCl	KI
10	1295	1157	828
25	1292	1286	1047
50	1024	1224	1315
75	404	668	643
100	1524	1099	1558
250	887	302	1327
500	1177	613	1193
1000	232	394	453

**Table S1.**

Scattering pattern numbers used for each type of electrolyte solution at different concentrations.

Concentration (mM)	LiCl	KCl	KI
10	1.0007	1.0016	1.0045
25	1.0018	1.0041	1.0112
50	1.0037	1.0081	1.0225
75	1.0055	1.0122	1.0337
100	1.0074	1.0162	1.0450
250	1.0185	1.0405	1.1125
500	1.0370	1.0810	1.2250
1000	1.0740	1.1620	1.4500

**Table S2.**

Water-solution balance coefficient for each type of electrolyte solution at different concentrations.